Mineralium Deposita
https://doi.org/10.1007/s00126-024-01248-5

ARTICLE

Influence of magmatic and magmatic-hydrothermal processes on the lithium endowment of micas in the Cornubian Batholith (SW England)

F. Putzolu[1] · R. Seltmann[1] · A. Dolgopolova[1] · R. N. Armstrong[1] · R. K. Shail[2] · J. Spratt[1] · Y. Buret[1] · C. Broderick[1] · W. Brownscombe[1]

Received: 18 June 2023 / Accepted: 22 January 2024

Abstract

The Cornubian Batholith (SW England) is an archetypal Variscan rare metal granite with potential for Li-mica mineralization. We present a petrographic, trace element and multivariate statistical study of micas from the Cornubian Batholith granite series and related hydrothermally altered units to assess the role of magmatic vs subsolidus processes and of fluxing elements (F and B) on the Li cycle during the evolution of the system. The mica types are as follows: (1) magmatic, which include Fe-biotite, protolithionite I and phengite-muscovite from the most primitive granites, and zinnwaldite I from more fractionated lithologies; (2) subsolidus, which encompass high-temperature autometasomatic Li-micas and low-temperature hydrothermal muscovite-phengite. Autometasomatic species include protolithionite II, zinnwaldite II and lepidolite, which were observed in the most fractionated and hydrothermally altered units, and occur as replacements of magmatic micas. Low-temperature hydrothermal Li-poor micas formed via alteration of magmatic and autometasomatic micas or as replacement of feldspars, and albeit occur in all studied lithologies they are best represented by the granite facies enriched in metasomatic tourmaline. The evolution of micas follows two major trends underlining a coupling and decoupling between the Li(F) and B fluxes. These include as follows: (1) a Li(F)-progressive trend explaining the formation of protolithionite I and zinnwaldite I, which fractionate Li along with Cs, Nb and Sn during the late-magmatic stages of crystallization, and of zinnwaldite II and lepidolite forming from the re-equilibration of primary micas with high-temperature Li-B-W-Tl-Cs-Mn-W-rich autometasomatic fluids; (2) a Li(F)-retrogressive trend explaining the low-temperature hydrothermal muscovitization, which represents the main Li depletion process. Trace element geochemistry and paragenesis of late muscovite-phengite support that muscovitization is a district-scale process that affected the upper parts of the granite cupolas through acidic and B(Fe-Sn)-saturated hydrothermal fluids associated with metasomatic tourmalinization, which were mixed with a low Eh meteoric component.

Keywords Lithium mica · Granite · Magmatic-hydrothermal transition · LA-ICP-MS · Cornubian Batholith

Introduction

The late-Variscan Cornubian Batholith (SW England) is a world-class example of a rare metal granite (RMG) system, with magmatic-hydrothermal Sn-Cu-W ores and with potential to produce Li from mica-type mineralization. The Cornubian Batholith includes several major plutons showing a pronounced variation in their macroscopic, mineralogical and geochemical features. Simons et al. (2016) described five granite types: G1 (two-mica granite), G2 (muscovite granite), G3 (biotite granite), G4 (tourmaline granite) and G5 (topaz granite). Many granite bodies from the Cornubian Batholith are hydrothermally altered and host locally mineralized units such as Sn- and W-greisen, banded Li-F-B

Editorial handling: R. L. Romer

✉ F. Putzolu
francesco.putzolu1@nhm.ac.uk

[1] Natural History Museum, Cromwell Road, London SW7 5BD, UK

[2] Camborne School of Mines, Department of Earth and Environmental Science, University of Exeter, Penryn Campus, Penryn TR10 9FE, UK

Published online: 19 February 2024

aplite-pegmatite complexes and porphyritic microgranite dikes (Halliday 1980; Antipin et al. 2002; Breiter et al. 2018; Uwanyirigira 2018). This diversity in facies, textural types and compositions of granite-related mineralization and alteration systems is due to late- and post-magmatic processes including fractionation and segregation of low-viscosity and volatile-rich melts, fluid-melt segregation and autometasomatism, and low-T hydrothermal alteration (Simons et al. 2016, 2017; Breiter et al. 2018). Peraluminous granites are commonly enriched in lithophile elements such as Li, Rb, Ta, Nb and Cs and bear significant amounts of late-magmatic to subsolidus mica-bearing assemblages (Černý et al. 2005).

The complex crystal structure of micas allows this group of phyllosilicates to host many trace elements through isomorphic and coupled substitutions (e.g. Tischendorf et al. 2001). Therefore, while in contact with evolving melts and/or fluids, micas easily re-equilibrate and fractionate the available elements (i.e. mostly large-ion lithophile element (LILE) and high field strength elements (HFSE)), thus acting as reliable archives of the mineralization history of magmatic-hydrothermal ore systems. For these reasons, mica-group minerals have been increasingly used as indicators to track the evolution of RMGs and related magmatic-hydrothermal units globally, and as a vector to the fertility of these systems (e.g. Martins et al. 2012; Legros et al. 2016; Breiter et al. 2019; Codeço et al. 2021; Guimarães et al. 2021; Monnier et al. 2022; Breiter et al. 2023). Lithium-bearing micas in the Cornubian Batholith were initially observed and described by the pioneering study of Cundy et al. (1960), whereas insights about the potential control of magmatic vs subsolidus processes on the variation of trioctahedral mica types have been given by Stone et al. (1988), Henderson et al. (1989), Stone (1992) and Müller et al. (2006). In this context, Simons et al. (2016; 2017) described variations in the mica mineralogy across the five granite types, but the assessment of the mica composition in selected plutons/facies of the Cornubian Batholith was limited. Features of micas occurring in some of the most intensively metasomatized units (e.g. greisen, aplite-pegmatite, porphyritic microgranite) were not included, and the alteration processes that affected the Li contents were not considered. Furthermore, due to analytical limitations, most of the previous authors described only the major and minor elements composition of granitic micas, thus providing little information on the trace element composition.

In this study, we present mineralogical and chemical data of micas by using a combined SEM, automated mineralogy, EPMA, LA-ICP-MS and multivariate statistics analytical protocol. Mica features were studied throughout the variably evolved granite members (G1 to G5), associated magmatic-hydrothermal units (i.e. aplite-pegmatite, greisen and porphyritic microgranite) and retrogressive alteration facies. Our objectives are as follows: (1) to understand the mineralogical and paragenetic evolution of micas in magmatic, magmatic-hydrothermal and retrogressive rock types within the Cornubian batholith; (2) to assess the influence of magmatic and subsolidus (autometasomatic and low temperature hydrothermal) processes on the endowment of Li and other ore metals (e.g. Cs, W, Nb, Ta and Sn) of the different mica types; and (3) to understand the processes that trigger the late Li remobilization and depletion in low-temperature retrogressive granite facies.

Geological setting

The Cornubian Batholith in SW England (Cornwall-Devon) covers an area 250-km long and 20–40-km wide (Fig. 1). South-west England lies within the European Variscan belt that formed following the late Devonian collision between Laurussia and Gondwana (ca. 370 Ma) (Kroner et al. 2007). The Cornubian granites were intruded into Devonian to Carboniferous sub-greenschist facies metasediments of the Rhenohercynian Zone. The hosting metasedimentary rocks were deposited in a passive margin setting and underwent deformation during the late Devonian through Carboniferous as a consequence of Variscan continental collision accompanying closure of the Rhenohercynian Ocean (Sanderson 1984; Durrance 1998; Shail and Leveridge 2009). The early-Permian magmatism that generated the Cornubian Batholith (293–275 Ma) was coeval with late- to post-orogenic NNW-SSE extension that reactivated Variscan thrust structures and triggered lithospheric thinning and mantle partial melting (Shail and Wilkinson 1994; Shail and Leveridge 2009; Simons et al. 2016; Alexander et al. 2019). This magmatic stage led to the emplacement of several composite peraluminous plutons, with the main bodies being the Dartmoor, St. Austell, Carnmenellis, Bodmin Moor, Tregonning-Godolphin and Land's End granites (Fig. 1).

Based on distinctive mineralogical characteristics, Simons et al. (2016) proposed a revised classification of the near-surface granite types of the Cornubian Batholith (Table 1):

- G1 two-mica granite: coarse- to fine-grained monzogranites consisting of 5 to 10 modal % trioctahedral micas, up to 6 modal % dioctahedral mica, subordinate tourmaline and a suite of accessory minerals. The main exposures of the G1 granites are located in the Carnmenellis, Bodmin and Isles of Scilly plutons.

- G2 muscovite granite: mineralogically similar to G1, with muscovite mica prevailing over biotite. The G2 granite mostly occurs as small stocks (e.g. Michael's Mount and Cligga Head). The G2 granite is spatially associated with W- and Sn-mineralized greisen-bordered veins.

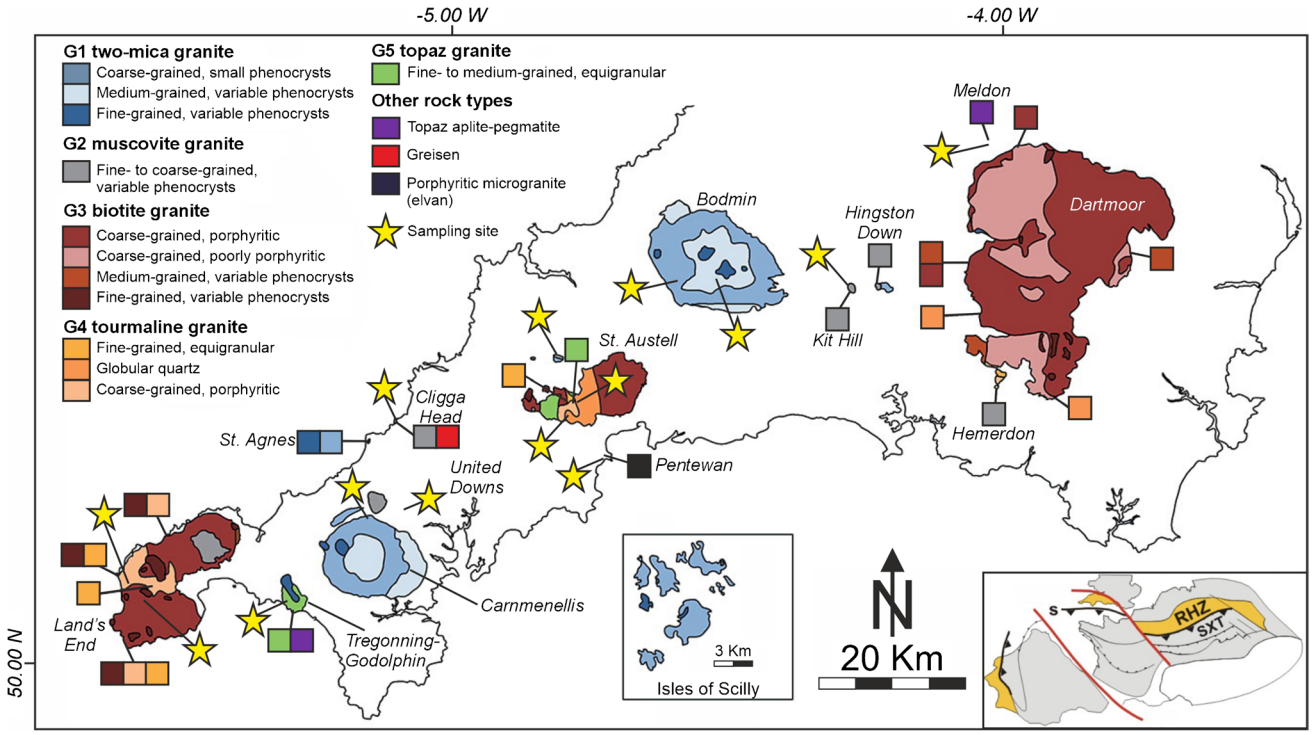

Fig. 1 Geological map of SW England (Cornwall-Devon) showing the near-surface granite types of the Cornubian Batholith according to the mineralogical classification of Simons et al. (2016). Please note: (1) squares indicate facies variations within each granite type, stars indicate sampling locations, while captions in italics indicate names of main locations for granite plutons and related rock types; (2) inset shows the G1 facies variation in the Isles of Scilly, which are located about 45 km west-southwest of the Land's End coast. Abbreviations: RHZ, Rhenohercynian Zone; SXT, Saxothuringian Zone; S, suture

- G3 biotite granite: coarse- to fine-grained porphyritic granites with approximately 10 modal % trioctahedral micas, minor tourmaline (up to 2.5 modal %) and minor muscovite. The main G3 exposure can be observed in the Land's End, Dartmoor and St. Austell localities.

- G4 tourmaline granite: tourmaline is the dominant ferromagnesian mineral with subordinate trioctahedral micas and abundant albite and alkali feldspars. The G4 granite occurs either as crosscutting sheets or as gradational contact with G3 granites in the Land's End, St. Austell and Dartmoor plutons. The G4 tourmaline granite displays the most pronounced facies variability (e.g. Manning et al. 1996). These include a magmatic facies with zinnwaldite and euhedral tourmaline, and a retrogressive facies with late dioctahedral micas (phengite + muscovite) plus a metasomatic tourmaline assemblage.

- G5 topaz granite: characterized by conspicuous topaz concentrations (up to 3 modal %) and by trioctahedral Li-micas. The best G5 exposures can be observed in the St Austell pluton, where the topaz granite forms sharp contact with G3 and G4.

Geochronological studies (i.e. Chesley et al. 1993; Clark et al. 1994) indicate that the G1 and G2 granites are the older lithologies, with ages of 291.4 ± 1.6–281.5 ± 1.6 Ma and 298.3 ± 4.6–279.3 ± 0.8 Ma, respectively. The G3 and G5 are the younger granites with ages of 281.8 ± 0.8–272.3 ± 1.8 and 281 ± 1.3 Ma, respectively, whereas geochronological data are not available for the G4 granite. The most recent petrogenetic model (Simons et al. 2016) inferred that most of the diversity of the granite types can be explained by fractional crystallization processes leading to the G1 → G2 and G3 → G4 magmatic series. The shift between the generation of G1 to G3 granitic melts has been explained by an increase in temperature that aided the transition from muscovite- to biotite-dominated partial melting of a mica-bearing greywacke source. Simons et al. (2016) also observed that the geochemistry of the G5 topaz granite cannot be explained by differentiation of the G1–G2 or G3–G4 series and proposed that it was generated by fluid-fluxed melting of a biotite-rich source rock in the lower crust.

Mineralization types associated with the Cornubian Batholith

The Cornubian Batholith hosts a large suite of granite-related magmatic-hydrothermal ores that formed from circulation of high-temperature fluids generated during the *syn*- and post-batholith emplacement (Scrivener 2006). The major

Table 1 Summary of the mica types detected in the Cornubian Batholith: a) micas in the granite series G1-G2, G3-G4 and G5, and in aplite-pegmatites and greisens; b) mica in the porphyritic microgranite

Section A			
Generation	Mica type	Alteration	Occurrence
Primary (late-magmatic)	Protolithionite I	Muscovitization, with local development of pseudomorphic chlorite	G1 two-mica granite, with minor relict grains in the G2 muscovite granite
	Muscovite I and phengite I	Muscovitization	G1 and G2 granites, subordinate in the G3 granite. Relict grains are also present in the greisens
	Fe-Biotite	Chloritization	G3 granite
	Zinnwaldite I	Alterated to zinnwaldite II and lepidolite, with extensive muscovitization and local chloritization	G4 granite. Relict grains are also found in the G5 granite and in the aplite-pegmatites
Secondary (autometasomatic)	Zinnwaldite II	Muscovitization	G5 topaz granite
	Protolithionite II	Muscovitization	Greisen
	Lepidolite	Muscovitization, altered to Li-phosphates (aplite-pegmatites)	G5 topaz granite and aplite-pegmatites
Secondary (hydrothermal)	Muscovite II and phengite II*	None	Detected in most of the studied lithologies. Developed in a lesser extent in the G3 biotite granite
	Muscovite III and phengite III*	None	Detected in most of the studied lithologies, but best developed in the G4 tourmaline granite
Section B			
Generation	Mica type	Alteration	Occurrence
Primary (magmatic-hydrothermal)	Zinnwaldite	Altered to lepidolite	porphyritic microgranite
	Muscovite*	None	
Secondary (autometasomatic)	Lepidolite	None	porphyritic microgranite
	Phengite*	None	

*Group including also the relatively Li-enriched counterparts (i.e., Li-muscovite and Li-phengite)

mineralization types include Sn-bearing magnetite ± sulfide skarns and quartz-tourmaline veins and breccias, W-Sn greisen (e.g. Cligga Head and St. Michael's Mount), fault and fracture-hosted Cu–Zn-As-Sn sulfide lodes (e.g. Chen et al. 1993; Scrivener 2006) and kaolinite China clay (e.g. Sheppard 1977). The onset of mineral exploitation in the study area dates back to the Bronze age, when mining activities targeted Sn and Cu, followed by a growth of the mining sector during the nineteenth century, making the Cornubian Ore Field a key district for base and precious metals and industrial minerals (Willis-Richards and Jackson 1989; Scrivener 2006). The ongoing rise in demand for Li resulted in major exploration surveys for Li in geothermal brines and in hard-rock (mica-type) ores (Gourcerol et al. 2019; Shaw 2022). Economic hard-rock Li resources in the Cornubian Batholith are primarily associated with the most fractionated granite member (i.e. G5 topaz granite) from the St. Austell pluton (Fig. 1). However, other extremely fractionated and hydrothermally altered units that can potentially host Li mineralization include aplite-pegmatite complexes, greisen deposits and porphyritic microgranite dikes (Table 1). Aplite-pegmatites are found in association with highly fractionated G5 topaz granites such as the Megiliggar Rocks leucogranite (Tregonning pluton), where banded aplite and pegmatite sills were emplaced at shallow depth into metasedimentary host rocks (Fig. 2a, b) (Simons et al. 2017; Breiter et al. 2018). The Meldon complex (Devon) is another example of a Li-, Nb, Ta- and B-and F-rich aplite-pegmatite (Figs. 1 and 2c); however, a spatial relationship with any fractionated granitoid has not yet been recorded, with the aplite-pegmatite body being located NW of the biotite-dominant (G3) Dartmoor pluton (Chaudhry and Howie 1973; Simons et al. 2017). Furthermore, small-scale pegmatoidal-aplitic facies (i.e. stockscheider) enriched in lepidolite and tourmaline are locally found in the G5 topaz granite in the St. Austell pluton (Fig. 2d, e). The autometasomatic alteration of the G2 muscovite granite stocks (St. Michael's Mount and Cligga Head) and locally of G5 topaz granite (St. Austell) resulted in W-Sn greisen, which contains minor Li-bearing micas (Jackson et al. 1977; Williamson et al. 1997). Greisen units consist of quartz infill veins bordered by late tourmaline haloes, and form sheeted metasomatic bodies crosscutting the granite stocks (Fig. 2f, g). Several stages of boron metasomatism have been observed in the Cornubian

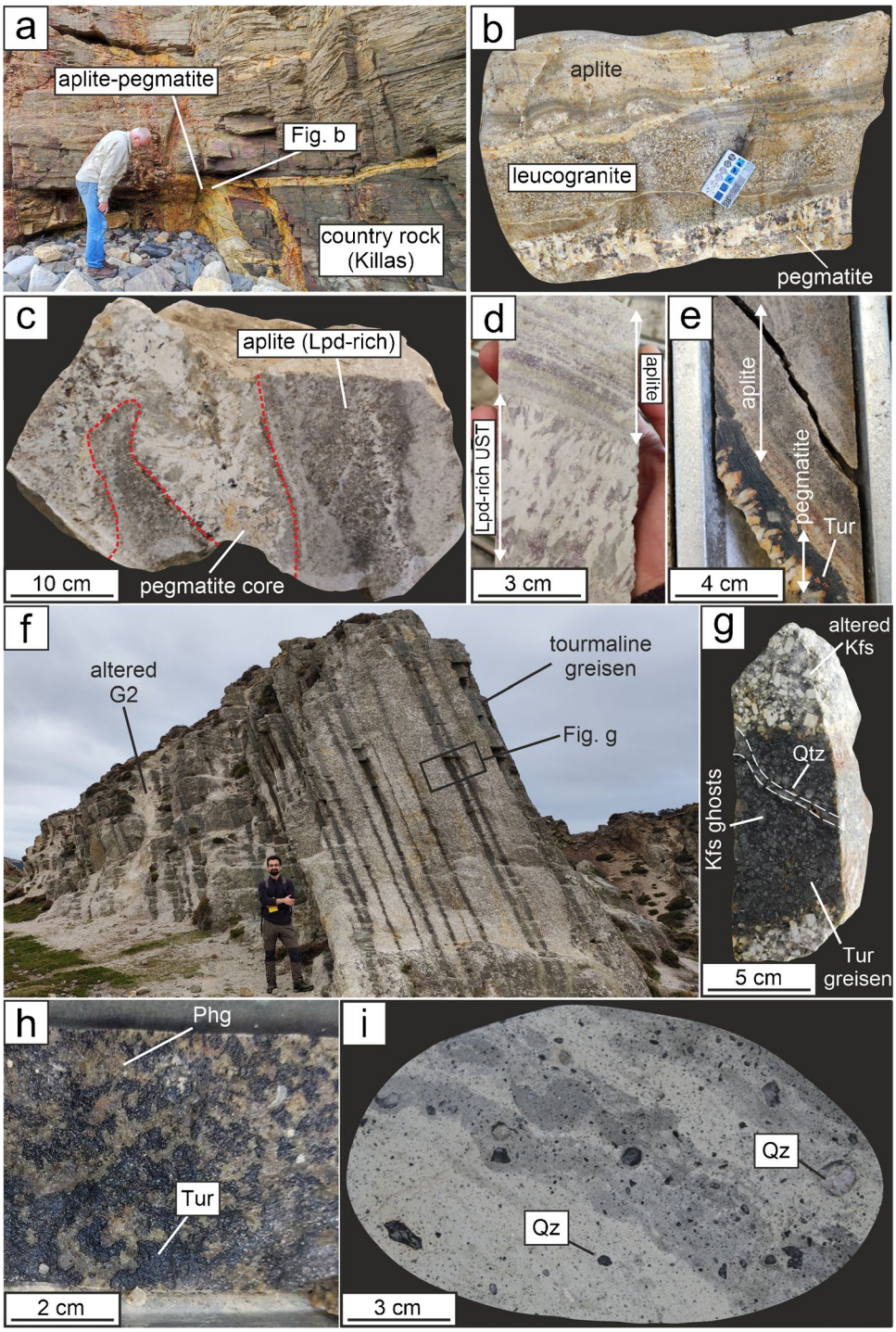

Fig. 2 **a** Megiliggar Rocks (Tregonning pluton) locality showing the contact between the aplite-pegmatite banded complex and the country rocks; **b** close-up view of a sample from Megiliggar Rocks showing banding of the leucogranite, pegmatite and aplite facies; **c** pegmatite and lepidolite-bearing aplite from Meldon; **d**, **e** aplitic-pegmatoid facies (stockscheider) in the G5 topaz granite at St. Austell; **f** greisen-bordered sheeted veins at Cligga Head; **g** tourmaline-quartz greisen from Cligga Head; **h** metasomatic tourmaline associated with green muscovite/phengite (muscovite alteration) in retrogressive facies of the G4 granite (St. Austell); **i** banded porphyritic microgranite. Abbreviations: Kfs, K-feldspar; Lpd, lepidolite; Qz, quartz; Phg, phengite; Tur, tourmaline; UST, unidirectional solidification texture

Batholith, resulting in the formation of tourmaline-bearing greisen units, replacement bodies, miarolitic cavities and breccia pipes (Williamson et al. 2010). Retrogressive facies in the G4 tourmaline granite contain a generation of metasomatic tourmaline that is closely associated with a pale green mica assemblage consisting of muscovite and/or phengite, which occur as a late and pervasive alteration of primary micas and feldspars (Fig. 2h). In the literature, this alteration facies has been described erratically, with a nomenclature varying between "phengite", "sericite" and "gilbertite" alteration (Meunier and Velde 1982; Psyrillos et al. 2001). Therefore, due to the complexities and controversies in describing alteration facies enriched in dioctahedral micas, in this present paper when referring to a specific member of the dioctahedral micas group, the proper mineral name is used (i.e. phengite vs muscovite), whereas the processes that formed post-magmatic dioctahedral

micas-bearing assemblages are referred to as "muscovitization" or "muscovite alteration". Porphyritic microgranite dikes (so-called "elvan" in historical literature) with potential to host rare metals are observed in steeply dipping extensional faults (Antipin et al. 2002) and have ages that overlap with those of the Cornubian Batholith (e.g. 288.7 ± 0.7 in dikes associated with the Carnmenellis pluton; Chesley et al. 1993). Porphyritic microgranites show a subvolcanic-like texture (Fig. 2i), which is likely produced by the abrupt drop in lithostatic pressure during the opening of deep-seated fractures and joints at the time of emplacement.

Material and analytical methods

A total of 30 samples were collected to cover the diversity of mica-bearing granite types (G1 to G5) and associated hydrothermally altered units (greisen, aplite-pegmatite and porphyritic microgranite) from the Cornubian Batholith (Fig. 1). Drill cores, old quarries and type localities including Land's End, Tregonning, St. Austell (i.e. Trelavour and Blackpool pits), United Downs, Cligga Head, Meldon and Pentewan were sampled (ESM1). The sampling strategy was aimed to collect granite and related hydrothermally altered units free of any Sn-W-Cu mineralization in order to reduce the influence of hydrothermal Sn-W-Cu mineralizing processes on the chemical signature of micas. The analytical work was conducted at the Image and Analysis Centre of the Natural History Museum, London (UK). Bulk-rock mineralogy, petrography and paragenesis were determined by X-ray powder diffraction (XRPD), automated mineralogy and scanning electron microscopy and energy dispersive spectrometry (SEM–EDS). The mica classification and their major and trace element characterization were determined through microchemical spot analysis and high-resolution elemental mapping using electron probe micro analysis (EPMA) and by laser ablation inductively coupled plasma mass spectrometry (LA-ICP-MS). The characterization of trace element patterns in micas was performed through statistical analyses, including principal component analysis (PCA), analysis of variance (ANOVA) and Tukey's HSD (honestly significant difference). Details about the analytical procedures are reported in ESM 2.

Results

Bulk-rock mineralogy and paragenesis

The G1 two-mica granite is dominated by coarse-grained quartz, K-feldspar and albite phenocrysts, with subordinate micas and euhedral late-magmatic tourmaline (Tur I) (ESM 3). Primary micas include protolithionite I and muscovite I occurring as poikilitic grains (Fig. 3a, b). A second generation of interstitial muscovite (Ms II) forms late overgrowth on protolithionite I (Fig. 3c).

The G2 muscovite granite mineralogy is similar to that of G1, but it contains more abundant primary muscovite and phengite (ESM 3). Li-micas are rare and only include minor relict protolithionite I (Fig. 3d). Later phengite is common and occurs as a replacement of primary micas (Phg II) and of feldspar grains (Phg III) (Fig. 3e, f).

Perthitic orthoclase with albite, quartz and micas characterize the G3 biotite granite (ESM 4). The dominant primary mica is Fe-biotite, which shows no clear evidence of muscovitization (Fig. 3g, h). Muscovitization in the G3 granite only resulted in newly formed muscovite (Ms III) occurring as infill of the intergranular spaces (Fig. 3i).

The retrogressive facies of the G4 tourmaline granite is characterized by globular quartz and by a potassic alteration consisting in late intergranular K-feldspars and pervasive muscovitization affecting feldspar (ESM 4). In this facies, tourmaline is present as a neo-formed generation that shows a Fe vs Mg zoning (Tur II) (Fig. 3j). The G4 units least affected by retrogressive mineral reactions contain relict primary Li-micas (Znw I) and subhedral late-magmatic tourmaline (Tur I) (Fig. 3k, l).

Quartz and K-feldspar are the dominant minerals in the G5 topaz granite. Alkali feldspars are overprinted by late muscovite, albite and kaolinite (ESM 5). Primary Li-micas consist of poikilitic zinnwaldite (Znw I) locally enclosing primary topaz (Tpz I) and apatite inclusions (Fig. 4a). Primary Li-micas micas are overprinted by late Fe-poor zinnwaldite (Znw II), lepidolite and phengite (Phg II) (Fig. 4b, c).

The aplite-pegmatite units (Meldon) are characterized by an interlocking quartz ± albite ± Li-mica ± K-feldspar assemblage, which locally develops unidirectional solidification textures (UST) that contain lepidolite (ESM 5). Lepidolite and K-feldspar are present to a lesser extent in the aplite layers, wherein topaz I, albite, apatite and Li-phosphates (montebrasite–amblygonite) are more abundant (ESM 5). Late mineralizing processes include the alteration of topaz I to a Li-chlorite (cookeite) plus fluorite assemblage (Fig. 4d), the alteration of primary phosphates (apatite and amplygonite-montebrasite) and lepidolite to late Li-phosphates (tancoite) (Fig. 4e), and the muscovitization of lepidolite (Fig. 4f).

The greisen units (Cligga Head, altered G2 granite) are dominated by rounded recrystallized quartz grains associated with late tourmaline, topaz and Li-micas (ESM 6). Lithium micas (protolithionite II) are associated with late topaz (Tpz II) and are mostly present as late phases filling voids and intergranular spaces between quartz grains (Fig. 4g). Protolithionite II is overprinted by late phengite (Fig. 4h). Relics of pre-greisen primary phengite are locally observed (Fig. 4i).

The porphyritic microgranites (Pentewan locality) consist of mica-rich aphanitic rocks with large cryptocrystalline quartz clusters embedded in a fine-grained

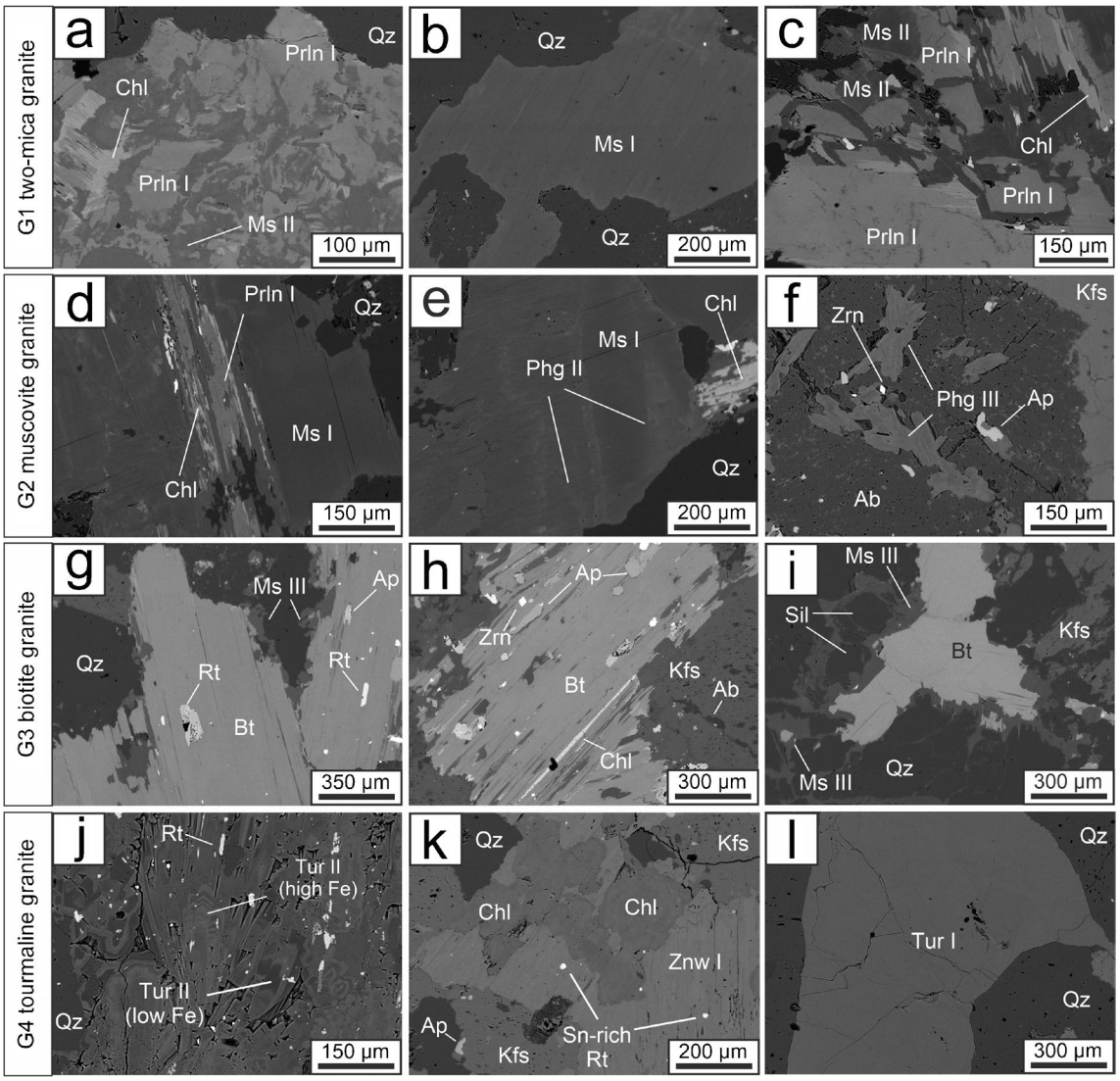

Fig. 3 Mineralogical and textural features of the G1 two-mica, G2 muscovite, G3 biotite and G4 tourmaline granites: (**a**) primary protolithionite (I) overgrown by late muscovite (II); (**b**) poikilitic primary muscovite (I); (**c**) primary protolithionite (I) overgrown by secondary muscovite (II); (**d**) Fe-chlorite pseudomorph after primary protolithionite (I) and muscovite (I); (**e**) primary muscovite (I) partially overprinted my secondary phengite (II); (**f**) feldspar altered by late phengite (III); (**g**, **h**) primary Fe-biotite with rutile, zircons and apatite inclusions; (**i**) late-muscovite (III) filling the cracks network within quartz, sillimanite-group minerals and biotite; (**j**) zoned secondary tourmaline (retrogressive G4 facies); (**k**) primary zinnwaldite (I) replaced by chlorite (magmatic G4 facies); (**l**) primary zinnwaldite (I) replaced by chlorite (magmatic G4 facies). Abbreviations: Ab, albite; Ap, apatite; Bt, Fe-biotite; Chl, chlorite; Kfs, K-feldspar; Ms, muscovite; Phg, phengite; Prln, protolithionite; Qz, quartz; Rt, rutile; Sil, sillimanite-group minerals; Tur, tourmaline; Zrn, zircon; Znw, zinnwaldite

muscovite-quartz groundmass (ESM 6). Note that a paragenetic linkage between micas from porphyritic microgranite and those from granite members is not evident so are treated separately (Table 1). Zinnwaldite, Li-muscovite and Li-phengite occur as phenocrysts and as rims on quartz, whereas late lepidolite forms rims on mica phenocrysts (Fig. 4j–l). Mineral inclusions of cassiterite and arsenopyrite are commonly found in micas (Fig. 4k, l).

Lithium mica characterization

Major element compositions Based on major element compositions determined by EPMA (ESM 7), micas belong to the following series: (1) Fe-biotite–siderophyllite–protolithionite; (2) zinnwaldite–lepidolite; and (3) ± Li-bearing muscovite–phengite (Fig. 5a). Two compositional vectors can be outlined, including as follows: a Li(F)-progressive trend,

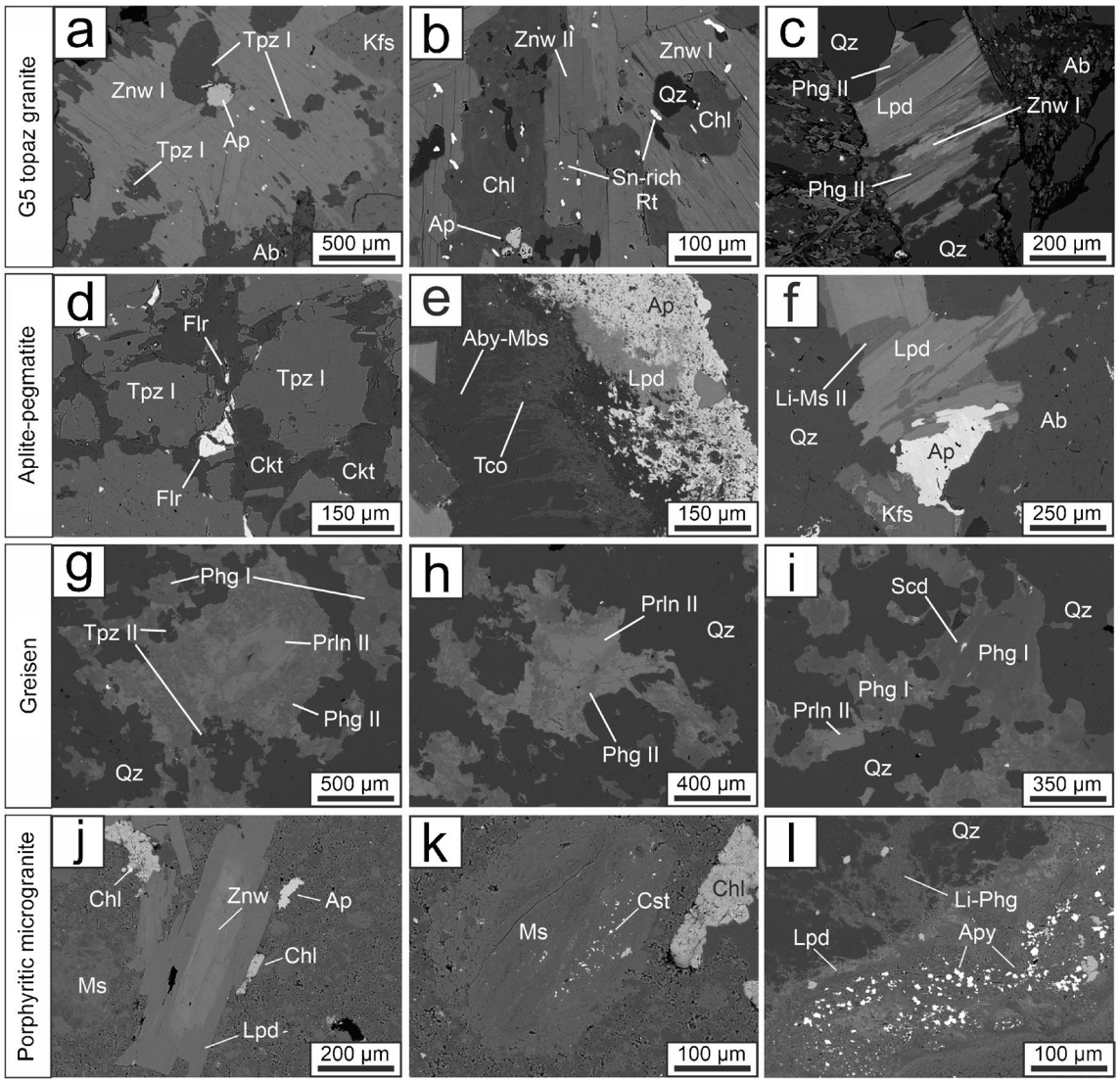

Fig. 4 Mineralogical and textural features of the G5 topaz granite, aplite-pegmatite, greisen and porphyritic microgranite: (**a**) poikilitic primary zinnwaldite (I) with topaz I inclusions; (**b**) primary zinnwaldite (I) replaced by late Fe-poor zinnwaldite (II); (**c**) zinnwaldite I replaced by late lepidolite and phengite II; (**d**) late fluorite and cookeite filling spaces in an altered topaz I grain; (**e**) late tancoite replacing amblygonite-montebrasite; (**f**) late Li-muscovite (II) overgrown onto lepidolite; (**g**) prolotolithionite II – phengite – topaz II intergrowth; (**h**) greisen protolithionite (II) replaced by secondary phengite (II); (**i**) greisen protolithionite (II) associated with primary and secondary phengite (I and II); (**j**) late lepidolite replacing a zinnwaldite phenocryst; (**k**) muscovite grain with cassiterite inclusions; (**l**) secondary lepidolite and Li-phengite rims surrounding quartz. Abbreviations: Ab, albite; Aby-Mbs, amblygonite-montebrasite; Ap, apatite; Apy, arsenopyrite; Chl, chlorite; Ckt, cookeite; Cst, cassiterite; Flr, fluorite; Kfs, K-feldspar; Lpd, lepidolite; Ms, muscovite; Phg, phengite; Prln, protolithionite; Qz, quartz; Scd, scorodite; Rt, rutile; Tco, Tancoite; Tpz, topaz; Znw, zinnwaldite

accounting for the chemistry of trioctahedral micas with an increasing Li concentration (i.e. Fe-biotite to lepidolite, trend "a" in Fig. 5a); and a late Li(F)-retrogressive trend describing the chemistry of dioctahedral species (i.e. ± Li-rich phengite and muscovite). The Li-retrogressive trend follows three discrete compositional (subvectors b, c, d; Fig. 5a). The zinnwaldite → muscovite trend includes Li-phengite forming as an intermediate product of the breakdown of the parental primary Li-mica (trend "b" in Fig. 5a). This chemical vector describes the muscovitization process in the most fractionated granite types, as well as in the greisen and porphyritic microgranite units. The lepidolite → muscovite trend results in the formation of Al^{VI}-rich micas that fall in the Li-muscovite field (trend "c" in Fig. 5a). This vector explains the alteration of Li-micas in the aplite–pegmatite units. The muscovite ⇆ phengite trend describes the late muscovitization of earlier micas and feldspars (trend "d" in Fig. 5a). This also accounts for the primary Li-free muscovite and phengite measured in G1 and G2. The Li contents of primary micas from the G1, G2 and G3 granites (Fe-biotite

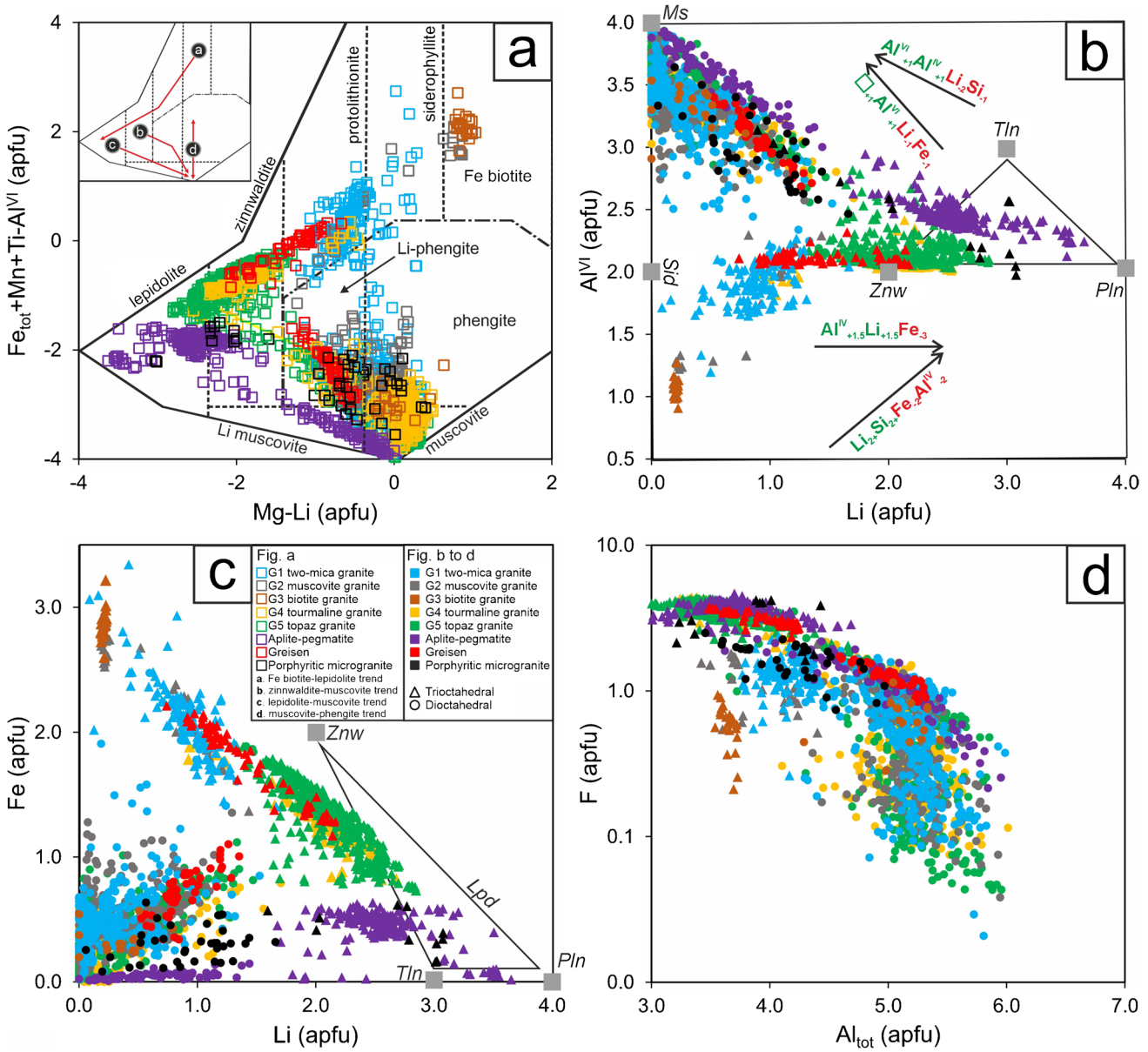

Fig. 5 EPMA data of lithium micas in the Cornubian batholith: (**a**) lithium micas classification diagram (modified after Tischendorf et al. 1997) highlighting the main evolutionary tendencies observed in different granites, aplite-pegmatites, porphyritic microgranites and greisens. Please note: data in the phengite and muscovite fields also include primary (magmatic) dioctahedral micas from the G1 two-mica and G2 muscovite granites; (**b**, **c**) Al^{VI} vs Li (apfu) and Fe_{tot} vs Li (apfu) plots showing the vectors of crystallographic substitution of trioctahedral and dioctahedral lithium micas (modified after Legros et al. 2016); (**d**) F (apfu) vs Al_{tot} (apfu) plot highlighting the variation in the fluorination degree between dioctahedral and trioctahedral mica species. Abbreviations: Lpd, lepidolite; Ms, muscovite; Pln, polylithionite; Sid, siderophyllite; Tln, trilithionite; Znw, zinnwaldite

and protolithionite I) correlate with a gain in octahedral Al (i.e. Al^{VI}) and loss of Fe^{2+} (Fig. 5b, c), whereas micas in the most evolved granite series (i.e. G4, G5), as well as in the aplite-pegmatite, greisen and porphyritic microgranite units, have a flat Li vs Al^{VI} trend (Fig. 5b). The Li concentration in muscovite, phengite and their Li-bearing counterparts is anticorrelated with Al^{VI} and Fe (Fig. 5c, b). The Al_{tot} gain resulting from muscovitization and Li downgrade correlates with a significant decrease of fluorine (Fig. 5d).

Trace element compositions Trace element compositional data (LA-ICP-MS) of the analysed mica species are reported in ESM 8. Micas from the Cornubian Batholith show high to detectable amounts of the following trace elements: B

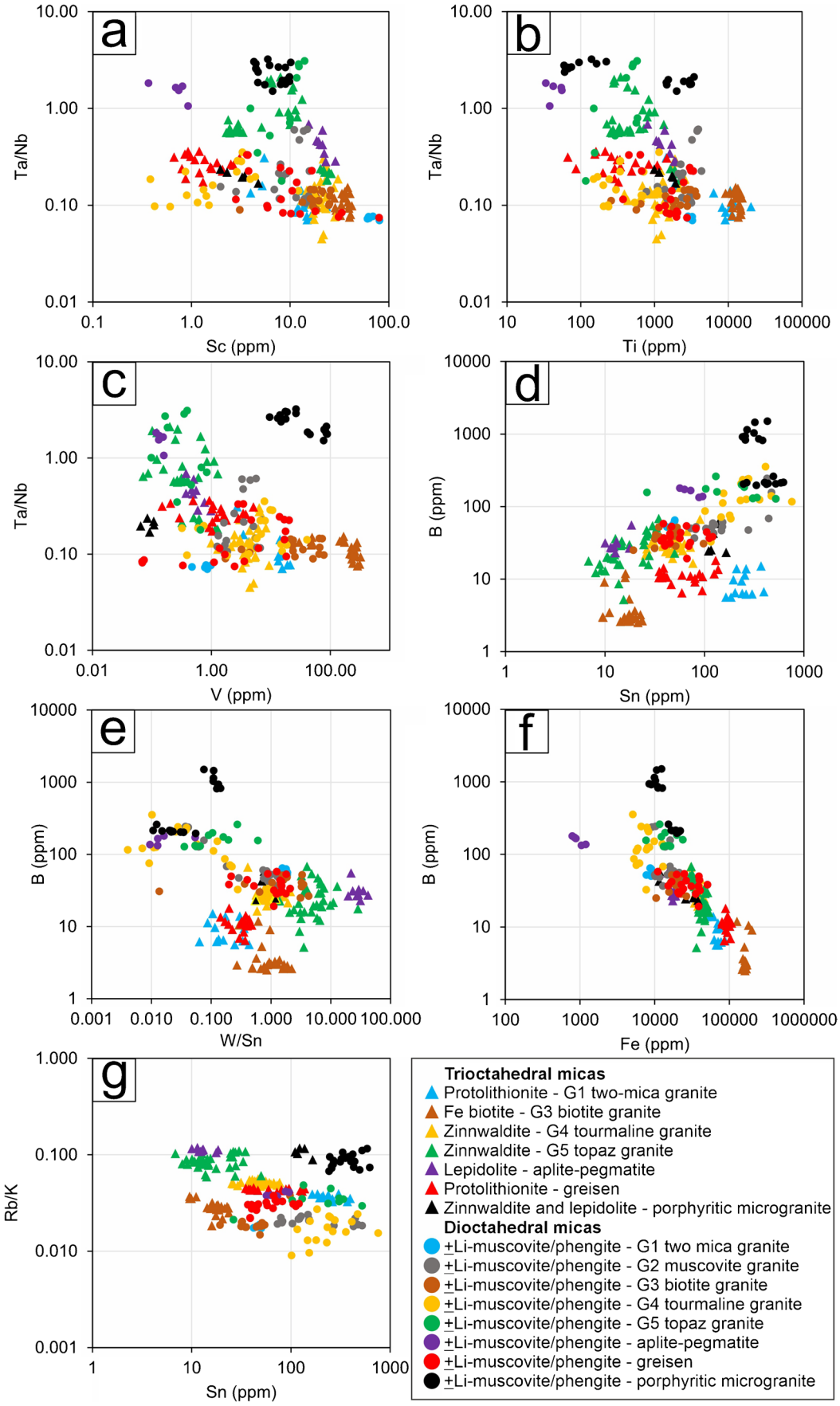
a
Ta/Nb
Sc (ppm)
b
Ta/Nb
Ti (ppm)
c
Ta/Nb
V (ppm)
d
B (ppm)
Sn (ppm)
e
B (ppm)
W/Sn
f
B (ppm)
Fe (ppm)
g
Rb/K
Sn (ppm)
Trioctahedral micas
Protolithionite - G1 two-mica granite
Fe biotite - G3 biotite granite
Zinnwaldite - G4 tourmaline granite
Zinnwaldite - G5 topaz granite
Lepidolite - aplite-pegmatite
Protolithionite - greisen
Zinnwaldite and lepidolite - porphyritic microgranite
Dioctahedral micas
±Li-muscovite/phengite - G1 two mica granite
±Li-muscovite/phengite - G2 muscovite granite
±Li-muscovite/phengite - G3 biotite granite
±Li-muscovite/phengite - G4 tourmaline granite
±Li-muscovite/phengite - G5 topaz granite
±Li-muscovite/phengite - aplite-pegmatite
±Li-muscovite/phengite - greisen
±Li-muscovite/phengite - porphyritic microgranite

◂**Fig. 6** **a–c** Relationship between the Ta/Nb ratio and Sc, Ti and V contents of micas. The observed trends record a progressive decrease in V, Ti and Sc coupled with an increase of the Ta/Nb ratio in micas from the more fractionated and hydrothermally-altered units (i.e. G4, G5, aplite-pegmatite and porphyritic microgranite); **d–g** Relationship between B vs Sn, B vs W/Sn, B vs Fe and Rb/K vs Sn contents of micas. The observed trends record a geochemical decoupling between subsolidus micas. Specifically, high-temperature autometasomatic trioctahedral micas (G5 topaz granite, aplite-pegmatites and porphyritic microgranite) show high Rb/K and W/Sn ratios, whereas low-temperature hydrothermal dioctahedral micas (from most of the studied lithologies) have high Sn-B and low Fe contents. Notes: *The dioctahedral category includes ± Li-bearing micas belonging to the muscovite and phengite groups

(2–1500 ppm), Sc (0.37–80 ppm), V (0.06–323 ppm), Ge (0.63–21 ppm), Ga (32–156 ppm), Nb (0.62–607 ppm), Sn (6–757 ppm), In (0.07–5 ppm), W (0.90–477 ppm), Ta (0.06–98 ppm) and Tl (3.79–70 ppm). LA-ICP-MS analysis was carried out to quantify with a higher resolution a series of elements also analysed through EPMA. These include Li (28–28,191 ppm), Na (161–8974 ppm), Ti (33–2044 ppm), Mn (77–20,133 ppm), Fe (789–201,132 ppm), Rb (898–11,174 ppm), Sr (0.02–46 ppm), Cs (36–7403 ppm) and Ba (0.04–558 ppm).

Primary protolithionite and Fe-biotite from G1 and G3 have the highest V, Sc and Ge contents (up to 323 ppm, 80 ppm and 21 ppm, respectively). A negative correlation between V, Sc and Ge concentration and Ta/Nb ratios has been observed in all granitoids (Fig. 6a–c). The highest concentrations of B and Sn (> 100 ppm), which are positively correlated with each other, occur in muscovite and phengite (Fig. 6d) from the most fractionated evolved granite members species and associated lithologies (i.e. G4, G5, aplite-pegmatite and porphyritic microgranites). A wide range of Sn contents are present in protolithionite and Fe-biotite micas in G1, G3 and in the greisen units—the measured Sn composition of protolithionite and Fe-biotite fall outside of the dominant Sn-B trend observed for the rest of micas (Fig. 6d). The B contents of micas are also negatively correlated with the W/Sn ratio and Fe contents (Fig. 6e, f).

The highest Rb/K ratios have been measured in zinnwaldite II and lepidolite from G5, aplite-pegmatite and porphyritic microgranite, with Rb/K values anticorrelated with Sn (Fig. 6g). Increasing Rb/K ratios positively correlate with Cs and Mn in zinnwaldite and lepidolite in the most fractionated lithologies (ESM 9). Late muscovite and phengite show decreasing trends of Rb/K and Li contents at increasing Na, In and B concentrations. An exception of this trend is recorded in muscovite from porphyritic microgranites that shows anomalously high Rb, Li and Cs concentrations (ESM 9). Micas in the studied granites show a peculiar geochemical coupling and decoupling of Li with the Ta-Nb and W-Sn geochemical pairs (ESM 10). Specifically, an enrichment of Li-Sn-W is recorded by primary Li-micas in the G1 granite (protolithionite I), whereas Li-micas from the G5 and aplite-pegmatite (zinnwaldite II and lepidolite) have high W but low Sn contents. Based on the W/Sn ratios, Sn is enriched compared to W (i.e. low W/Sn ratios) primarily in dioctahedral micas, whereas high W/Sn ratios occur only in zinnwaldite II and lepidolite from the topaz G5 granite and the aplite-pegmatite units. Tantalum and Nb behave similarly to the W-Nb pair. Specifically, high Nb and Ta contents occur in primary Li micas from G1 and G4, whereas a Ta enrichment over Nb is observed in late micas from the G5 granite, aplite-pegmatite and porphyritic microgranites. Noteworthy, the transition between zinnwaldite I and II occurring from G4 to G5 is characterized by an increase of the W/Sn, Ta/Nb and Rb/K ratios (ESM 9, 10).

Trace element zoning in micas Combined EPMA and LA-ICP-MS elemental mapping indicates that the transition from primary zinnwaldite (Znw I) to replacive lepidolite in the topaz G5 granite and aplite-pegmatite units (Fig. 7a–f and 7g–l, respectively) is characterized by an increase of Li and F contents that correlates with an increase of the Ta/Nb and W/Sn ratios. The alteration of the zinnwaldite plus lepidolite assemblage is marked by a Li and F loss and results in the formation of Sn-rich phengite and development of native Cu inclusions within mica grains and along cleavage planes (Fig. 7e, f). Caesium in the fractionated units (e.g. aplite-pegmatite) is concentrated in late lepidolite rims developed from the alteration of primary Ti-bearing zinnwaldite (Fig. 7l). In the retrogressive facies of the G4 granite and in the greisen units (Fig. 8a–f and 8g–l, respectively), the Li loss associated with muscovitization is also correlated with a decrease of the Fe and F contents and with an increase of the Sn and B concentrations in the late muscovite plus phengite assemblage. The alteration and Li(F) leaching from primary micas is associated with the formation of late fluorine and boron minerals (i.e. fluorite and tourmaline II).

Discussion

Paragenetic and compositional evolution of lithium micas in the Cornubian Batholith

The variations in mineralogy, paragenesis and chemistry of lithium micas in the Cornubian Batholith (Table 1 and Fig. 9) broadly follow those observed in other RMG- and pegmatite-related Li occurrences worldwide (e.g. Martins et al. 2012; Legros et al. 2016; Breiter et al. 2019; Codeço et al. 2021; Guimarães et al. 2021; Monnier et al. 2022). The following mica types were identified (Table 1 and Fig. 9):

- Primary trioctahedral and dioctahedral micas, which have variable amounts of lithium. Based on their textural and paragenetic characteristics (poikilitic grains interlocked with

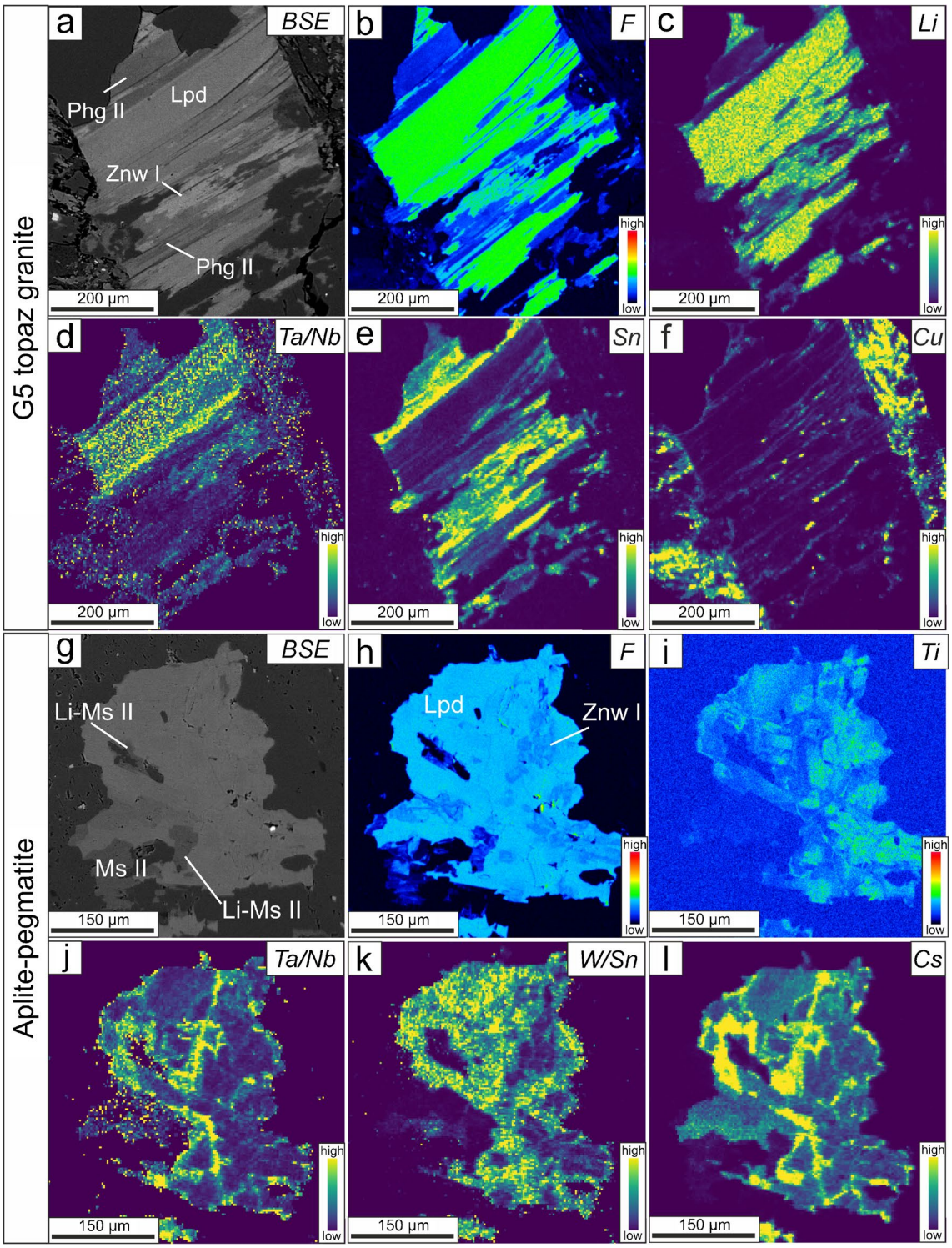

Fig. 7 EPMA and LA-ICP-MS elemental maps of mica assemblages from the G5 topaz granite (a–f) and from the aplite-pegmatite units (g–l). **a–f** Magmatic zinnwaldite replaced by autometasomatic lepidolite and by hydrothermal phengite. Formation of replacive lepidolite is correlated with an increase of the Ta/Nb ratio, while muscovitization with Li, and F losses and enrichments of Sn and Cu; **g–l** Magmatic zinnwaldite replaced by autometasomatic lepidolite and by hydrothermal phengite. Metasomatic alteration increased the Cs and F concentrations, and the Ta/Nb and W/Sn ratios in the late lepidolite. Abbreviations: Lpd, lepidolite; Ms, muscovite; Phg, phengite; Znw, zinnwaldite

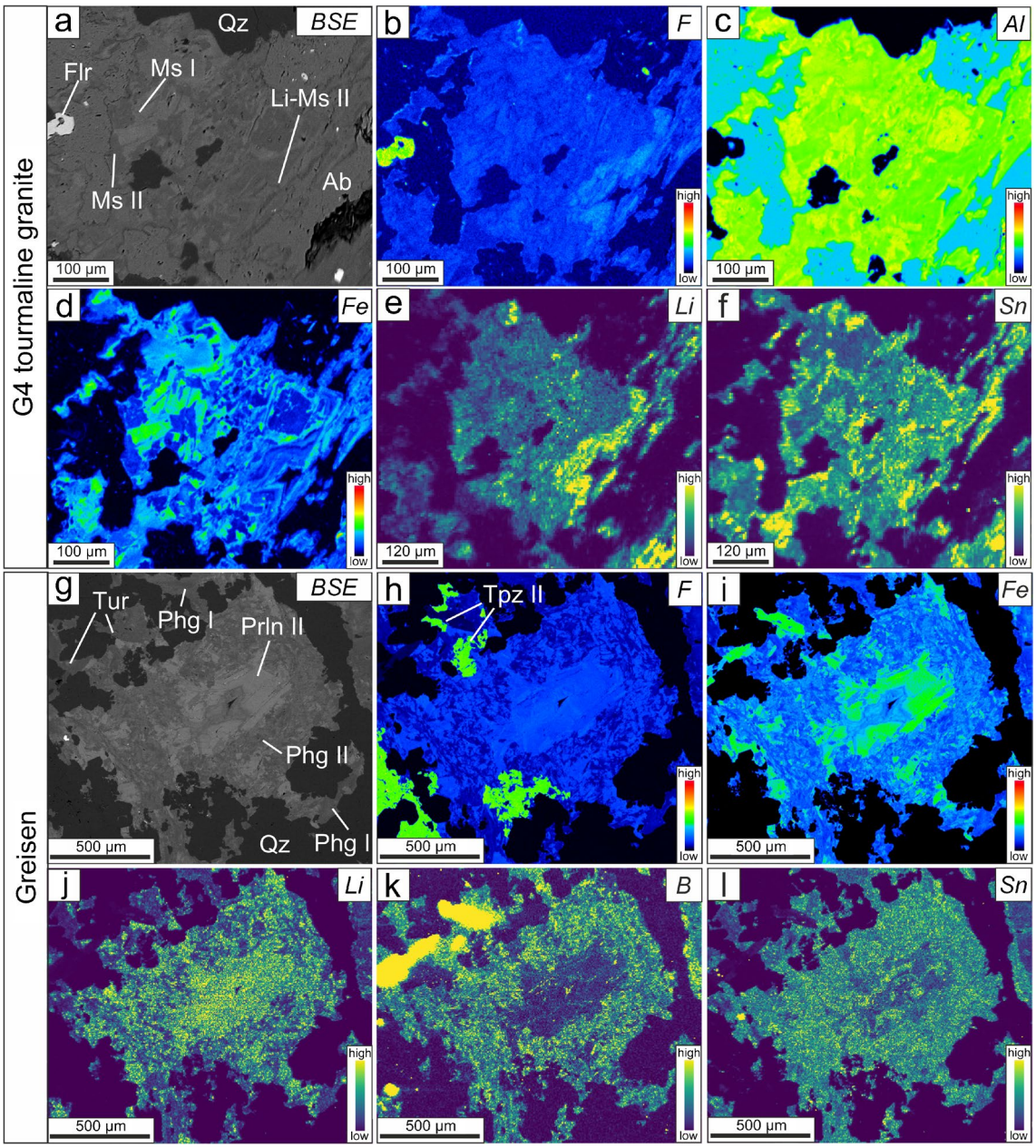

Fig. 8 EPMA and LA-ICP-MS elemental maps of mica assemblages from the retrogressive facies of the G4 tourmaline granite and the greisen unit. **a**–**f** Magmatic muscovite replaced by hydrothermal muscovite in the G4 tourmaline granite. Formation of hydrothermal muscovite is marked by a Fe loss and Sn gain; **g**–**l** Phengite II plus protolithionite II assemblage replacing primary dioctahedral micas in the greisen units (g–l). Formation of late phengite is associated with a loss of Li, F and Fe and with increase in B and Sn. Abbreviations: Ab, albite; Flr, fluorite; Ms, muscovite; Phg, phengite; Prln, protolithionite; Qz, quartz; Tpz, topaz; Tur, tourmaline

quartz and feldspars), they formed during the late-magmatic stages of crystallization. Lithium-free late-magmatic micas include muscovite I and phengite I that occur primarily in the oldest and least fractionated members of the magmatic series (G1 and G2 granites) as well as Fe-biotite in G3 granite. Lithium-rich late-magmatic micas include protolithionite I in the G1 granite and zinnwaldite I in the G4 granite and in lesser amounts in the G5 granite and in the aplite-pegmatite units. Subordinate primary Li-rich micas are also found as zinnwaldite phenocrysts in the porphyritic microgranite units, although as discussed in the following sections their origin cannot be ascribed to purely late-magmatic processes as for the rest of the granite units.

- Secondary micas include species formed under subsolidus conditions and show a higher degree of diversity in terms of lithium contents, paragenesis and conditions

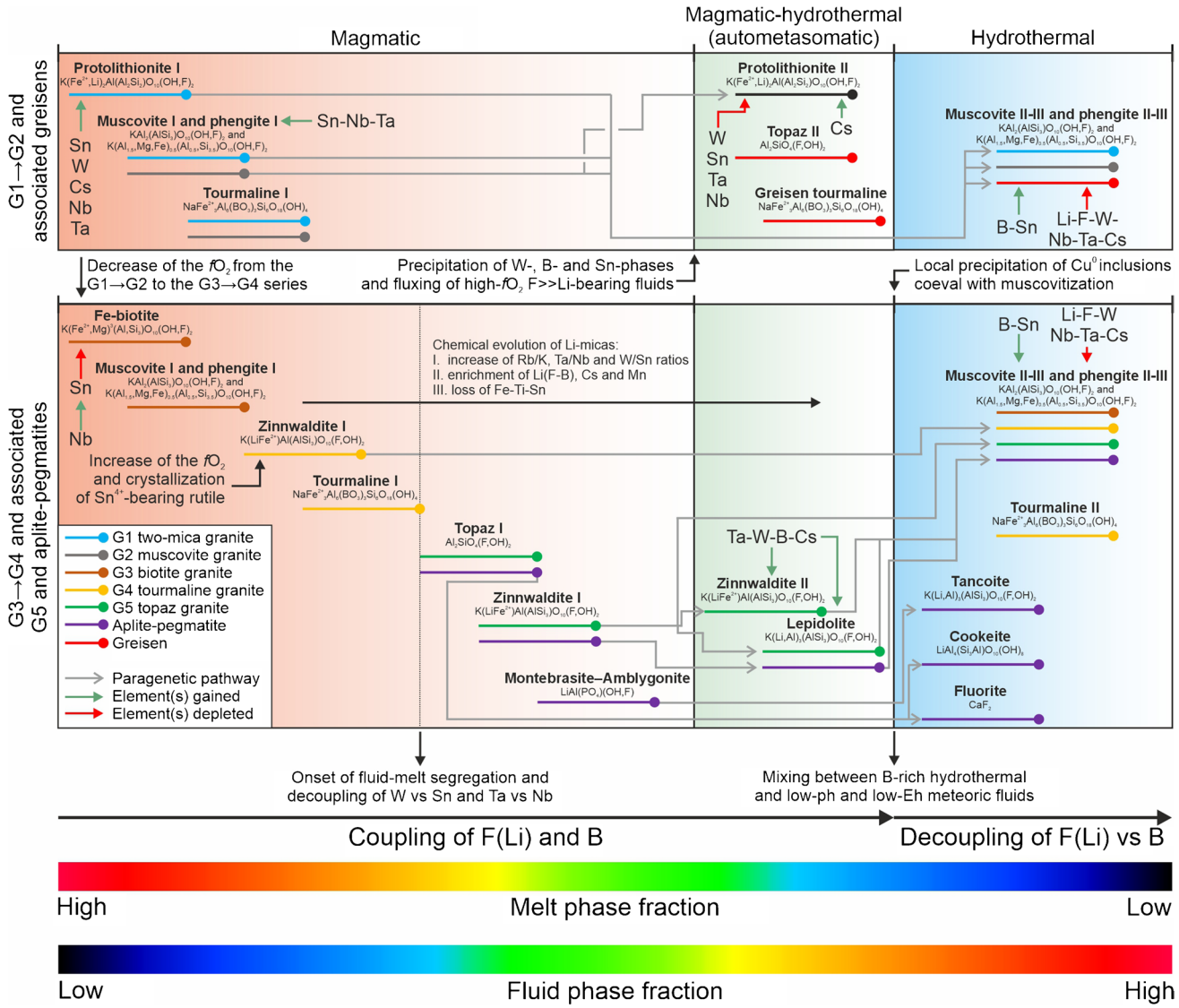

Fig. 9 Paragenetic chart showing the evolution of lithium micas and non-mica Li-, F- and B mineral repositories. Mica paragenesis is also displayed in relationship with the fluxing of F and B, and with the gain and depletion in rare metals (Cs, Nb, Ta, W and Sn). Specifically: (1) magmatic fractionation processes that originated the G1→G2 and G3→G4 granite series resulted in enrichments of Li, F and B in micas of the biotite to zinnwaldite series, and in enrichments of Sn and Cs in protolithionite I and Nb, Ta, Sn in magmatic dioctahedral micas; (2) autometasomatic alteration led to the formation of zinnwaldite II and lepidolite in the most fractionated lithologies (i.e. G5 and pegmatite). This process led to a further enrichment of Li, F, B and Cs, as well as to a rise of the Ta/Nb, W/Sn and Rb/K ratios autometasomatic micas; (3) low-temperature muscovitization originated dioctahedral micas (i.e. muscovite and phengite) through alteration of magmatic to autometasomatic Li(F)-mica and feldspars. This process triggered a partial Li leaching from most granite types and a Sn and B enrichment in the late muscovite and phengite. Please note: upper panel represents the micas evolution in the G1→G2 granite series and associated greisen units; lower panel summarizes the micas evolution in the G3→G4 granite series and associated G5 granite and aplite-pegmatites

of formation. Secondary Li-micas form replacement of existing primary micas and occur in lithologies that have experienced high-temperature autometasomatism under volatile- and/or water-saturated conditions at the time of formation. These include the mica assemblages of lithologies that are typically described as deeply altered through high temperature fluids, such as the protolithionite II associated with a late topaz + tourmaline + quartz assemblage in the greisen units, and Li-rich phengite forming rims on cryptocrystalline quartz in the porphyritic microgranite units. Noteworthy, secondary Li-micas were also observed in the G5 topaz granite and in the aplite-pegmatite units, where the distinction between melt- and fluid-buffered processes is still a matter of scientific debate. For example, despite the presence of relicts primary micas in cores of mineral grains, these micas are replaced by later generations of zinnwaldite

(Znw II) and lepidolite (Figs. 4b and 7), thus indicating re-equilibration with an exsolved fluid component. Secondary Li-depleted micas include phengite and muscovite as well as their Li-bearing counterparts. This mica type includes replacive micas after primary Li-rich species and micas forming pervasive alteration halos due to feldspar alteration. The former type is present in most of the studied granites and associated formations, whereas pervasive muscovitization is best developed in association with metasomatic tourmaline (Tur II) in the retrogressive facies of the G4 granite (Fig. 9).

The above mica groups show significant differences in terms of Li concentrations, major and trace elements compositions. The relationship between Li and major elements (i.e. octahedral cations as Al^{VI} and Fe) can be used as a crystal chemistry proxy of the major mechanisms of Li accommodation in the crystal lattice (e.g. Foster 1960; Roda Robles et al. 2006; Legros et al. 2016). The observed Li vs Al^{VI} relationships in micas from the Fe-biotite and lepidolite end-members indicate that the Li enrichment is associated with a loss of bivalent octahedral cations following the $1.5Al^{IV} + 1.5Li^{+} \leftrightarrows 3Fe^{2+}$ and $2Li^{+} + 2Si^{4+} \leftrightarrows 2Fe^{2+} + 2Al^{IV}$ crystallographic vectors (Fig. 5b). The muscovitization of the earlier Li-micas assemblage is explained by the combination of two substitution vectors that collectively account for the Al_{tot} (i.e. $Al^{VI} + Al^{IV}$) enrichment and Li downgrade observed in late muscovite and phengite (Fig. 5b). In G1, G2 and G4, the Li depletion through muscovitization is linked with a Fe loss due to the $\square + Al^{VI} \leftrightarrows Li^{+} + Fe^{2+}$ substitution in the octahedral sheet, while the muscovitization of zinnwaldite and lepidolite from G5, greisen**,** porphyritic microgranites and from the aplite–pegmatite follows an Al_{tot} gain through the coupled $Al^{IV} + Al^{VI} \leftrightarrows 2Li^{+} + Si^{4+}$ substitution (Fig. 5b).

The trace element compositions of micas (LA-ICP-MS) were used to carry out principal component analysis (Fig. 10) to identify geochemical patterns among different mica types. The PCA iterations were carried out on different groups: (1) PCA on trioctahedral species (i.e. Fe-biotite to lepidolite); (2) PCA on dioctahedral species (i.e. muscovite, phengite and Li-bearing counterparts); (3) PCA on the combined mica datasets (i.e. trioctahedral and dioctahedral). In iteration 1 (Fig. 10a, b), PC1 and PC2 collectively account for about 60% of the explained variance (ESM11). The PC1 distinguishes Li-rich and Li-poor mica species. Li-poor primary micas from the least fractionated granites spread towards negative PC1 values and show correlations with the Sr-Ba-Ge group in the case of protolithionite I (G1 granite) and with the V-Ti-Sc-Nb group in the case of Fe-biotite (G3 granite). Lithium-micas from the most fractionated units (G4, G5, aplite-pegmatite and porphyritic microgranite units) are distributed along positive PC1 values and display a correlation with the W-Rb-Tl-B group. The PC2 explains the chemistry of Li-micas in the greisen units (protolithionite II) and to a lesser extent those in the G1 granite (protolithionite I), which are correlated with the Sn-In-Mn-Cs group. In the iteration 2 (Fig. 10c, d) the PC1 and PC2 collectively explain about 55% of the variance in the dataset (ESM12). Primary muscovite and phengite in the G1 and G2 granites, as well as relict primary micas in the greisen units, correlate with the Na-Ge-Sc-Nb-W-Ti-Mn group. Secondary muscovite and phengite cluster away from the primary mica group along negative PC1-PC2 values owing to their enrichment in Ba, Sr, Sn, B. Lithium-rich phengite and muscovite from the porphyritic microgranite units have a unique trace element signature and stand out from the rest of the data due to their high contents of Cs, Li, Rb, Li, Sn and Ta. Iteration 3 (Fig. 10e, f) provides a summary of the contrasting chemical compositions of all micas: PC1 accounts for the chemical decoupling between Li-F micas (zinnwaldite and lepidolite), which have a Li-W-Tl-Cs-Mn-W-Tl association, and muscovite/phengite, which are correlated with the B-Sn-In-Sr-Ba-Na group. A slight decoupling between primary and secondary dioctahedral micas can be observed. Specifically, primary micas in G1, G2, G3 and in the greisen show a V-Na-Ba-Sr footprint, while secondary micas in the most fractionated lithologies have a Sn-B footprint. The PC2 differentiates the least fractionated micas (i.e. biotite and protolithionite) based on their variable endowment of Ge, Ga, Nb, Sc and V.

The statistical difference between mica groups clustered by the PC1 and PC2 in the PCA iterations 1 and 2 was further assessed through the ANOVA and the Tukey's HSD tests (see ESM 2 for method description). The ANOVA test resulted in *p*-values below 0.05 for the principal components (i.e. PC1 and PC2) used to discriminate the observed mica groups in the trioctahedral and dioctahedral datasets (ESM 11, 12, respectively). The pairwise comparisons of trioctahedral mica groups (ESM11) support the statistical diversity and the singular chemical signature of most mica species (*p*-adjusted values < 0.05). It is worth mentioning that limited statistical similarities (*p*-adjusted values > 0.05) were detected for zinnwaldite and lepidolite from highly fractionated and metasomatized rock types (i.e. G5 topaz granite, aplite-pegmatite and porphyritic microgranite units). Noteworthy, although the ANOVA test on dioctahedral micas supported the grouping of PCA, the pairwise comparisons carried out by the Tukey's HSD test indicate a larger statistical similarity in the identified muscovite and phengite groups (ESM12).

Trace element footprint of micas: a window into magmatic vs subsolidus processes

The earliest formed micas detected in the G1 → G2 and G3 → G4 magmatic series are protolithionite I (G1) and Fe-biotite (G3) (Fig. 9). These mica species occur as non-zoned

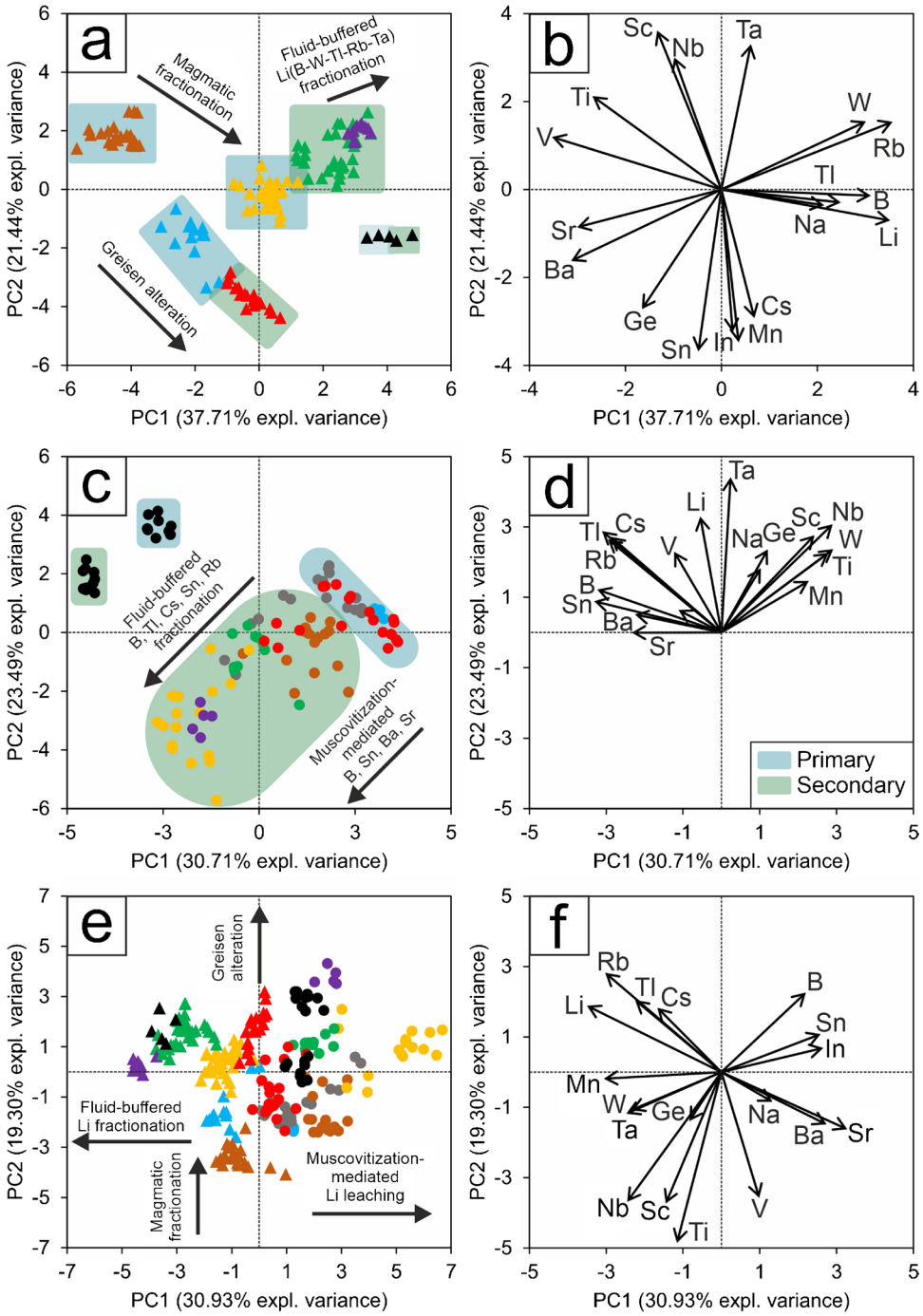

Fig. 10 **a**, **b** PC1 vs PC2 biplots showing the PCA results for trioctahedral micas; **c**, **d** PC1 vs PC2 biplots showing the PCA results of principal component analysis for dioctahedral micas; **e**, **f** PC1 vs PC2 biplots showing the PCA results for the combined mica datasets. Notes: *The dioctahedral category includes ± Li-bearing micas belonging to the muscovite and phengite groups (see Fig. 6 for colour and symbol legend)

homogenous grains (e.g. Figure 3a, g), indicating little or no re-equilibration with later melt batches and/or with exsolved fluids; thus, their trace-element footprints are representative of the composition of the parental granitic melts. Protolithionite I and Fe-biotite are variably enriched in Nb, Cs and Ta (ESM 9, 10), which is in line with the incompatible behaviour of these elements in peraluminous granitic melts (e.g. Icenhower and London; 1995; Evensen and London 2003; Michaud et al. 2021). However, there are some differences in their Sn contents, with Sn preferentially enriched in primary protolithionite from the G1 granite (Fig. 6d). The Sn contents in Fe-biotite from the G3 granite contrast with the reported higher Sn values of biotite from other RMG provinces (e.g. Zinnwald-Cínovec, Johan et al. 2012; Breiter et al. 2019). The low Sn contents in Fe-biotite can be ascribed to more reducing conditions in the most primitive G3 melts (Fig. 9), allowing Sn to be fractionated in fluids as Sn^{2+} through complexing with F^- and OH^-, rather than being fixed in magmatic micas in its tetravalent form (i.e. Sn^{4+}) (Eugster 1985; Lehmann 1990; Halter et al. 1996;

Lehmann 2021). Previous studies on the Cornubian Batholith have proposed that the fractionation of a biotite + feldspar + REE-phase assemblage can explain the petrogenesis of the G3 → G4 series and formation of late-magmatic Li-micas (e.g. Stone 1992; Ward et al. 1992; Darbyshire and Shepherd 1994; Müller et al. 2006; Simons et al. 2016). The trace element compositions of micas presented here can be used to test this hypothesis and to shed light on the role of purely magmatic vs subsolidus processes. Micas from the Cornubian Batholith are enriched in HFSE, and therefore they have potential to act as mineral competitors with columbite-tantalite, wolframite and cassiterite for Nb, Ta, W and Sn fractionation during the magmatic-hydrothermal processes (Zhu et al. 2018; Breiter et al. 2019; Yang et al. 2020; Guimarães et al. 2021; Monnier et al. 2022). Specifically, the Sn-W and Nb–Ta geochemical pairs have a contrasting behaviour during the fluid segregation from a melt, with Ta and W experiencing a higher partitioning towards the fluid phase producing subsolidus mineralogical assemblages with high W/Sn and Ta/Nb ratios (e.g. Audetat and Heinrich 2000; Ballouard et al. 2016). Based on LA-ICP-MS data, no significant differences exist in the Ta/Nb and W/Sn ratios of Fe-biotite and zinnwaldite I (ESM 10), supporting the hypothesis that a magmatic process can explain the proposed G3 → G4 fractionation. Furthermore, Fe-biotite is an important Ti repository in the G3 granite, whereas zinnwaldite I from G4 is depleted in Ti (Fig. 6b) and is commonly associated with Sn-bearing rutile inclusions (Fig. 3k). This suggests that the magmatic lithium enrichment during the G3 → G4 fractionation was characterized by increasing conditions of the oxygen fugacity of the evolved melt that allowed the Ti(Sn^{4+}) fractionation in magmatic oxides (Fig. 9). The changing oxidation conditions of the melt during the G3 → G4 fractionation can also explain the observation made by previous studies that concluded that despite the fact that in the Cornubian Batholith the crystallization of late-magmatic tourmaline is confined to granitic facies originated from a melt batch sufficiently enriched in Fe(Mg), no significant magmatic tourmaline is found in the most primitive G3 granite (e.g. London and Manning 1995).

The observed mica evolution from G3 to G4 (i.e. biotite-zinnwaldite series; Fig. 9) follows crystallographic vectors that indicate a Li fractionation in zinnwaldite I concurrent with a loss of Fe and Mg (Fig. 5a–c). This is in agreement with experimental work of Pichavant (2022) that indicates removal of mafic components in peraluminous melts is necessary to achieve the Li(F)-saturation and to crystallize late-magmatic Li-micas assemblages. However, petrographic evidence in this study indicates that zinnwaldite I and tourmaline I coexist in the late-magmatic G4 granite assemblage (Fig. 3k, l). This suggests that G3 → G4 fractionation in the Cornubian Batholith did not exhaust all the ferromagnesian components and that suppression of biotite crystallization, followed by the stabilization of Fe(Mg)-poor micas (zinnwaldite I), enabled the residual Fe and Mg to behave as incompatible elements and to fractionate in the final B-bearing melt batches, eventually leading to the crystallization of tourmaline I.

The latest petrogenetic models of Simons et al. (2016, 2017) proposed that the Li(F)-endowed G5 topaz granite originated from the fluid-flux mediated melting of a biotite-bearing source rock that generated a low viscosity and low solidus temperature melt, which underwent extreme feldspar fractionation to form a Li-mica + albite + topaz + quartz assemblage. Our new petrographic data show that late-magmatic phases, including poikilitic zinnwaldite I, as well as idiomorphic topaz and apatite inclusions in mica, are present in the G5 assemblage (Fig. 4a), thus partially supporting this model. However, the presence of zoned micas consisting of zinnwaldite I cores overprinted by late zinnwaldite II and lepidolite (Fig. 4b, c) indicates that primary micas re-equilibrated with an exsolved fluid, and thus that a purely magmatic process alone cannot fully explain the Li-endowment of G5. Further evidence of the role of fluid-buffered processes in the G5 evolution are given by the trace element signatures of micas. Specifically, pseudomorphic Li-micas in the topaz G5 show a sharp increase of the Ta/Nb and Rb/K ratios that correlates with an increase in W and with a loss of Ti if compared to primary Li micas in G5 and G4 units (Figs. 6b and 7a–f, ESM 9, 10). A similar paragenetic and chemical evolution of Li-micas has been observed in the zoned micas from pegmatite-aplite units (Fig. 7g–l), where the presence of subsolidus mineralogical assemblages (i.e. cookeite + tancoite + fluorite; Fig. 4d, e) is due to a hydrothermal overprint of the magmatic assemblage (Fig. 9). Further evidence of the role of a fluid component during evolution of the G5 and aplite-pegmatite units is the preferential enrichment of Cs in late mica rims that developed on primary mica cores (Fig. 7g–i). The development of Cs-rich rims indicates that behaviour of Cs in the most evolved formations is different to that observed in magmatic protolithionite (G1–G2 series) and is controlled by its fractionation into aqueous solutions relative to crystals or melt, as recently documented by the experimental work of London (2022).

Lithium micas in the porphyritic microgranites have high Rb/K and Ta/Nb (Fig. 6b, g) indicating a strong influence of a fluid component at the time of emplacement. This is in agreement with observations of Henley (1974) and Antipin et al. (2002), who suggested that porphyritic microgranites formed through hybrid melts mixed with a significant juvenile fluid component enriched in lithophile elements. In the studied porphyritic microgranites, a paragenetic association between mica phenocrysts and cassiterite inclusions has been observed (Fig. 4k), whereas secondary Li(F)-micas show a significant W depletion compared to species observed in formations with a similar hydrothermal

influence (i.e. G5 and aplite-pegmatite; ESM 10). This could indicate that porphyritic microgranites were re-equilibrated with a fluid that preferentially extracted W, producing a Sn-W geochemical decoupling. A similar footprint has been observed in hydrothermal micas from the Karagwe-Ankole granite-pegmatite belt (Rwanda), and was ascribed to W extraction from diluted metamorphic fluids supplied by the sedimentary country rocks (Hulsbosch et al. 2016) and is in line with the findings of Wilkinson (1990), who indicated that during the emplacement of the Cornubian Batholith, exsolved magmatic-hydrothermal fluids have mixed with a meteoric-metamorphic fluid component derived from the Devonian to Carboniferous metasedimentary rocks.

Greisen alteration of the G2 muscovite granite resulted in the breakdown of the magmatic feldspar ± muscovite assemblage, forming secondary Li-micas (protolithionite II) and high-temperature hydrothermal topaz and tourmaline (Fig. 4g and 8g–l and ESM 6). The subsolidus origin of greisen protolithionite is evidenced by its occurrence as void fillings within secondary quartz (ESM 6) and by the lack of V, Sc and Ti (Fig. 6a–c) that are characteristic of magmatic micas from the G1 to G3 granites (i.e. protolithionite I and Fe-biotite). Compared to the parental magmatic muscovite, greisen protolithionite is enriched in Li, Mn, Cs and Rb; depleted in B, W, Sn, Ta and Nb; and has lower W/Sn and Ta/Nb ratios (ESM 9, 10). We propose that this chemical evolution is primarily controlled by the fO_2 of the system during autometasomatism, which in turn dictates the nature of competing minerals precipitating in the greisen assemblage and the rare metals fractionation between micas and non-mica mineral repositories. Specifically, the breakdown of primary muscovite to greisen protolithionite is closely associated with the formation of scorodite ($Fe^{3+}AsO_4{\cdot}2H_2O$) (Fig. 4i). As evidenced by the pioneering experimental work of Dove and Rimstidt (1985), scorodite formation requires extremely high Eh conditions of fluids, even higher than the Eh levels required by Fe-oxy-hydroxides to form in the critical zone. Therefore, its stability in the greisen assemblage implies the mixing between F-rich and low-pH metasomatizing fluids exsolved during the cooling of the granitic body and the meteoric water reservoirs that were effective in creating oxidative conditions. The high Eh conditions favoured the formation of scheelite + wolframite + cassiterite ores and of metasomatic tourmaline, and although these minerals were not detected in the studied samples, they are known to be conspicuous in the greisen units from the Cornubian Batholith (Campbell and Panter 1990; Williamson et al. 1997). Therefore, the formation of the scheelite + wolframite + cassiterite assemblage during the greisen alteration generated a Sn, W and B-depleted fluid that precipitated protolithionite II, a process similar to that observed in other Variscan granites (e.g. Beauvoir granite, France; Monnier et al. 2022). The Li-Sn-W mineralized greisens that developed in other Variscan systems such as in the Zinnwald-Cínovec (Germany and Czech Republic) and in the Beauvoir (France) granites display a Li-mica assemblage consisting of zinnwaldite ± lepidolite formed shortly after autometasomatic topaz (Breiter et al. 2019; Monnier et al. 2022). In this respect, the Cornubian greisens are unique in that high-temperature autometasomatic processes resulted in more "primitive" Li-micas (i.e. protolithionite) coeval with high-temperature hydrothermal topaz. This indicates that despite the F-rich nature of autometasomatic fluids during the greisen episode, they were least fractionated compared to greisen fluids in other RMGs. This yielded only a partial Li enrichment of primary micas and formation of relatively late topaz, which represents a by-product of the mineralizing process originating from the high F/Li ratio of the system. The least fractionated nature of greisen fluids in the Cornubian Batholith is also evidenced by the trace element compositions of greisen protolithionite, which is relatively poor in Ta, W, Rb and Tl compared to secondary Li(F)-micas in the G5, aplite-pegmatite and porphyritic microgranite units (ESM 9, 10, Fig. 10a).

Li endowment and late muscovitization of micas: role of F vs B fluxes

Late-magmatic and subsolidus Li micas in the Cornubian Batholith show Li enrichment trends closely linked to the fractionation of F, Rb and a suite of rare metals including W, Sn, Ta, Nb and Cs (Fig. 9), which is a feature identified in most peraluminous Li-F granites and LCT pegmatites worldwide (e.g. Martins et al. 2012; Legros et al. 2016; Breiter et al. 2019; Codeço et al. 2021; Guimarães et al. 2021; Monnier et al. 2022; Breiter et al. 2023). However, in this study, we have observed that the Li supercharging through late-magmatic and subsolidus processes, and the later Li loss through muscovitization, is also closely linked to boron fluxing at several stages during the batholith evolution (Fig. 9). Specifically, secondary Li(F)-micas are present in tourmaline-free formations that experienced a significant fluid overprint (i.e. G5, aplite-pegmatite and porphyritic microgranite units). These Li-micas (i.e. zinnwaldite II and lepidolite) show anomalous concentrations of B and a Li-B-W-Ta-Rb-Tl-Na chemical fingerprint (Fig. 10a, b). This implies that high-temperature subsolidus processes generating Li-mica assemblages are characterized by a geochemical coupling between Li, F and B, which is in agreement with the experimental work of London (1986) that illustrates a Li-F-B coupling during the magmatic-hydrothermal evolution of granitic and/or pegmatitic systems. Specifically, if tourmaline crystallization is suppressed, B can be fractionated in high pH fluids in the form of Li-tetraborate species ($Li_2B_4O_7$) that, similarly to F, can act as fluxing components thus decreasing the solidus temperatures and triggering the

depolymerization of hydrous silicate melts (London 1986). This process could easily explain the endowment of Li-F-B and rare metals in subsolidus mica assemblages in tourmaline-poor formations in the Cornubian Batholith and in other RMG districts worldwide.

The behaviour of Li, F and B changes during late muscovitization, which represents the dominant post-Li enrichment process that occurred during latest stages of the hydrothermal history of the batholith. As opposed to the Li-F-B geochemical coupling observed for the Li(F)-progressive trend, muscovitization was driven by fluids that have generated a geochemical decoupling between F(Li) and B. Specifically, muscovitization is the main trigger of the Li and F leaching from magmatic and subsolidus Li-micas (Fig. 5a, d). Muscovitization affected most of the units in the Cornubian Batholith; however, this process is best developed in the retrogressive G4 granite facies dominated by a metasomatic tourmaline along with green phengite/muscovite assemblage (Fig. 2h and ESM 4). Trace element mapping (Figs. 7 and 8) and PCA (Fig. 10c–f) indicate that muscovitization triggers a significant Fe, Li and F loss from primary mica, coincident with a Sn, B, Ba and Sr enrichment in late muscovite and/or phengite. The close association between muscovitization and metasomatic tourmaline and the trace element footprint of muscovite/phengite can be explained through the late P–T-pH evolution of the batholith. Specifically, at low P–T conditions, metasomatic tourmaline forms when the system is Fe-saturated and when the boron coordination (i.e. ^{IV}B vs ^{III}B) is dominated by trigonal species (London 1986). Under these conditions, the formation of tourmaline releases acids to the systems. The Fe loss produced from alteration of primary and secondary Li-micas (e.g. Figures 5c and 8d) may have been the main trigger to the Fe-saturation in the fluid necessary to precipitate metasomatic tourmaline, which in turn buffered the pH towards acidity favouring further extensive muscovitization. Furthermore, Pichavant (1981) has shown that decreasing pressure favours trigonal boron species (i.e. ^{III}B), thus triggering metasomatic tourmalinization at shallow depths. Another indicator of the relative of depth formation of the tourmaline ± phengite/muscovite assemblage is the Sn-enrichment recorded in secondary dioctahedral micas (Figs. 6g, 7e and 8f, l). Enrichment of Sn in late muscovite/phengite has been observed in other RMGs such as Zinnwald-Cínovec (Germany and Czech Republic) and Beauvoir (France) (Breiter et al. 2019; Monnier et al. 2022), and has been ascribed to late alteration processes that produced subsolidus assemblages including Sn-bearing muscovite in upper granite cupolas. The source of the fluids responsible for muscovitization fluids has not been previously assessed, but based on the evidence presented for the Cornubian Batholith, we propose that the flux of low-temperature hydrothermal fluids associated with metasomatic tourmalinization is a potential fluid source. Additionally, other evidence points to the presence of a lower temperature and possibly meteoric fluid component that may have affected the Cornubian Batholith on a regional scale. Muscovitization locally resulted in the formation of native Cu inclusions and/or laths along cleavage planes of mica grains (Fig. 7f), a similar process to that observed in biotite and chlorite in the supergene zones of porphyry Cu and of Ni-Cu-PGE sulfide deposits (Ilton and Veblen 1988 and 1993; Suárez et al. 2011). Interestingly, in these systems, the origin of native copper is explained through interaction of primary mica assemblages with low-Eh meteoric fluids that allowed Cu^{2+} initially hosted in trace amounts in primary micas to be reduced following the oxidation and release of the octahedral Fe (i.e. $2Fe^{2+} + Cu^{2+} \rightarrow 2Fe^{3+} + Cu^{0}$, Ilton et al. 1992)—a process of Fe release that we have systemically recorded for the transformation of Li-micas to muscovite and/or phengite. The low-Eh of meteoric fluids is also in agreement with the features of the Cornubian Batholith, where low-temperature alteration was limited to kaolinitization, with no clear development of oxy-hydroxide-bearing saprolite as expected under high-Eh supergene conditions (e.g. Freyssinet et al. 2005). Further evidence that subsolidus muscovitization was partly driven by an external fluid component sourced on a district scale (i.e. meteoric water) is given by multivariate statistical analyses. Specifically, the Tukey's HDS test indicates only a minor statistical difference between the chemical signature of secondary muscovite and phengite (ESM12), which support that these mica types re-equilibrated with a similar fluid regardless of the chemistry and facies of the granite of origin. The above observations indicate that late muscovitization, accountable for the Li(F)-downgrading in the Cornubian Batholith, is a post-magmatic and district-scale process that affected the upper parts of the granite cupolas, and occurred during the cooling and potentially during exhumation of the system and was aided by low-pH fluids resulting from a hydrothermal component deriving from metasomatic tourmalinization mixed with a low Eh meteoric component.

Conclusions

The mineralogical, paragenetic and trace element characteristics of micas in the G1 to G5 granites and associated rock types (i.e. aplite-pegmatite, greisen and porphyritic microgranite) from the Cornubian Batholith illustrate the relationship between the processes of lithium endowment and the enrichment/depletion of rare metals (i.e. Sn, W, Ta, Nb), LILE (Rb, Cs etc.) and fluxing elements (i.e. F and B). The main findings are summarized as follows:

- Late-magmatic to high-temperature autometasomatic processes are responsible for the fractionation of Li in Fe-biotite to lepidolite end-members. The Li enrichment

occurs concurrently with the fractionation of Rb, F, B, W, Tl, Cs, Mn, W and Tl and with the increase of the Rb/K, Ta/Nb and W/Sn ratio. This footprint suggests an increasingly conspicuous involvement of a fluid component in the most evolved rock types (i.e. G5, aplite-pegmatite and porphyritic microgranite), which in conditions of saturation of fluxing elements (i.e. F and B), allowed a decrease in the solidus temperatures, a depolymerization of hydrous silicate melt and the fractionation of rare metals.

- Late muscovitization, resulting in the breakdown of earlier micas and K-feldspars and in the formation of muscovite/phengite, is the main Li ore disruptive process in the Cornubian Batholith because it triggers a significant Li(F) depletion of the parental micas. The late generation of Li-poor muscovite/phengite has a B-Sn-Sr-Ba-Na geochemical signature, and although it is best represented in the retrogressive facies of the G4 tourmaline granite, it has been observed in most of the granite members. Paragenesis and geochemistry of late muscovite/phengite indicate that muscovitization is a subsolidus and district-scale process that likely occurred at shallow depth, during and/or after the exhumation of the batholith. Muscovitization probably is triggered by low-temperature hydrothermal fluids that were produced by tourmalinization, which were mixed with a low Eh meteoric component.

- Lithium micas control the partitioning of rare metals (i.e. Sn, W, Nb, Ta and Cs) across the magmatic to hydrothermal history of the Cornubian Batholith. Purely magmatic processes may enrich Nb, Cs and Ta in the most primitive micas (i.e. protolithionite I and Fe-biotite) in the least fractionated granite members (i.e. G1 two-mica granite and G3 biotite granite). The magmatic fractionation of Sn is controlled by the fO_2 of the orthomagmatic systems, allowing Sn^{4+} to be fractionated in the more oxidized G1 → G2 series. The s*yn*- to post-magmatic fluid-crystal segregation acts as a buffer for the fractionation of W, Cs, Sn and Ta in subsolidus mica assemblages. Our study also reports the highest documented Cs enrichment in micas (7400 ppm in Li-phengite from porphyritic microgranite), as well as high enrichment in Sn (760 ppm Sn in muscovite from the G4 tourmaline granite) and W (477 ppm in lepidolite from the aplite-pegmatite units).

Supplementary Information The online version contains supplementary material available at https://doi.org/10.1007/s00126-024-01248-5.

Acknowledgements The authors are grateful to Cornish Lithium Plc and British Lithium for granting access to open pits areas and drillcore material, to the personnel of the Image and Analysis Centre (Natural History Museum, London) for the help during the analytical work and to the Li4UK team for their field sampling campaign work. This paper benefited from the constructive comments of Karel Breiter and of the Editor in Chief and Associated Editor of Mineralium Deposita (Karen Kelley and Rolf Romer, respectively).

Funding This study received funding from the NERC Lithium for Future Technology LiFT (ID: NE/V007068/1) and Li4UK projects. This is also a contribution of AD and RS to project No. AP14870387 "Assessment of the lithium potential of Kazakhstan, criteria controlling deposit formation and guiding exploration" funded by the Ministry of Science and Higher Education of the Republic of Kazakhstan.

Declarations

Conflict of interest The authors declare no competing interests.

References

Alexander AC, Shail RK, Leveridge BE (2019) Late Paleozoic extensional reactivation of the Rheic-Rhenohercynian suture zone in SW England, the English Channel and Western Approaches. Geol Soc London, Special Publ 470:353–373. https://doi.org/10.1144/SP470.19

Antipin VS, Halls C, Mitichkin MA, Scott P, Kuznetsov AN (2002) Elvans of Cornwall (England) and Southern Siberia as subvolcanic counterparts of subalkalic rare metal granites. Russ Geol Geophys 43:847–857

Audetat AD, Heinrich CA (2000) Magmatic-hydrothermal evolution in a fractionating granite: a microchemical study of the Sn-WF-mineralized Mole Granite (Australia). Geochim Cosmochim Acta 64:3373–3393. https://doi.org/10.1016/S0016-7037(00)00428-2

Ballouard C, Poujol M, Boulvais P, Branquet Y, Tartèse R, Vigneresse JL (2016) Nb-Ta fractionation in peraluminous granites: a marker of the magmatic-hydrothermal transition. Geology 44:231–234. https://doi.org/10.1130/G37475.1

Breiter K, Ďurišová J, Hrstka T, Korbelová Z, Vašinová Galiová M, Müller A, Simons B, Shail RK, Williamson BJ, Davies JA (2018) The transition from granite to banded aplite-pegmatite sheet complexes: an example from Megiliggar Rocks, Tregonning topaz granite, Cornwall. Lithos 302:370–388. https://doi.org/10.1016/j.lithos.2018.01.010

Breiter K, Hložková M, Korbelová Z, Vašinová Galiová M (2019) Diversity of lithium mica compositions in mineralized granite–greisen system: Cínovec Li-Sn-W deposit, Erzgebirge. Ore Geol Rev 106:12–27. https://doi.org/10.1016/j.oregeorev.2019.01.013

Breiter K, Vašinová Galiová M, Hložková M, Korbelová Z, Kynický J, Costi HT (2023) Trace element composition of micas from rare-metal granites of different geochemical affiliations. Lithos 107135. https://doi.org/10.1016/j.lithos.2023.107135

Campbell AR, Panter KS (1990) Comparison of fluid inclusions in coexisting (cogenetic?) wolframite, cassiterite, and quartz from St. Michael's Mount and Cligga Head, Cornwall. England Geochim Cosmochim Acta 54:673–681. https://doi.org/10.1016/0016-7037(90)90363-P

Černý P, Blevin PL, Cuney M, London D (2005) Granite-related ore deposits. In: Hedenquist JW, Thompson JFH, Goldfarb RJ, Richards J.P. (Eds.), Economic Geology 100th Anniversary Volume, Society of Economic Geologists, Littleton, CO, pp 337–370 https://doi.org/10.5382/AV100.12

Charoy B (1886) The genesis of the Cornubian batholith (South-West England): the example of the Carnmenellis pluton. J Petrol 27:571–604. https://doi.org/10.1093/petrology/27.3.571

Chaudhry MN, Howie RA (1973) Lithium–aluminium micas from the Meldon aplite, Devonshire, England. Mineral Mag 39:289–296. https://doi.org/10.1017/minmag.1973.039.303.05

Chen Y, Clark AH, Farrar E, Wasteneys HAHP, Hodgson MJ, Bromley AV (1993) Diachronous and independent histories of plutonism and mineralization in the Cornubian Batholith, southwest England. J Geol Soc 150:1183–1191. https://doi.org/10.1144/gsjgs.150.6.1183

Chesley JT, Halliday AN, Snee LW, Mezger K, Shepherd TJ, Scrivener RC (1993) Thermochronology of the Cornubian Batholith in southwest England: implications for pluton emplacement and protracted hydrothermal mineralisation. Geochim Cosmochim Acta 57:1817–1835. https://doi.org/10.1016/0016-7037(93)90115-D

Clark AH, Chen Y, Farrar EBN (1994) Refinement of the time–space relationships of intrusion and hydrothermal activity in the Cornubian Batholith. Abstract volume Ussher Society Annual meeting, 345, Minehead

Codeço MS, Philipp W, Trumbull RB, Van Hinsberg V, Pinto F, Lecumberri-Sanchez P, Schleicher AM (2021) The imprint of hydrothermal fluids on trace-element contents in white mica and tourmaline from the Panasqueira W-Sn–Cu deposit. Portugal Miner Deposita 56(481–508):481–508. https://doi.org/10.1007/s00126-020-00984-8

Cundy EK, Windle W, Warren IH (1960) The occurrence of zinnwaldite in Cornwall. Clay Miner 4:151–156

Darbyshire DPF, Shepherd TJ (1994) Nd and Sr isotope constraints of the origin of the Cornubian Batholith, SW England. J Geol Soc 151:795–802. https://doi.org/10.1144/gsjgs.151.5.0795

Dove PM, Rimstidt JD (1985) The solubility and stability of scorodite, $FeAsO_4 \cdot 2H_2O$. Am Min 70:838–844

Durrance EM (1998) The pre-Devonian tectonic framework In: Selwood, E.B., Durrance, E, Bristow CM (Eds.) The geology of Cornwall. Exeter: Exeter University Press

Eugster HP (1985) Granites and hydrothermal ore deposits: a geochemical framework. Mineral Mag 49:7–23. https://doi.org/10.1180/minmag.1985.049.350.02

Evensen JM, London D (2003) Experimental partitioning of Be, Cs, and other trace elements between cordierite and felsic melt, and the chemical signature of S-type granite. Contrib to Mineral Petrol 144:739–757. https://doi.org/10.1007/s00410-002-0426-x

Foster MD (1960) Interpretation of the composition of lithium micas. U.S. Geological Survey Professional Paper 354B:11–49

Freyssinet P, Butt CRM, Morris RC, Piantone P (2005) Ore-forming processes related to lateritic weathering. Econ Geol 100th Anniv. Vol. 681–722. https://doi.org/10.5382/AV100.21

Good AJJ (1973) The mode of intrusion of Cornish elvans. Rep Inst Geol Sci 73:1–8

Gourcerol B, Gloaguen E, Melleton J, Tuduri J, Galiegue X (2019) Re-assessing the European lithium resource potential – a review of hard-rock resources and metallogeny. Ore Geol Rev 109:494–519. https://doi.org/10.1016/j.oregeorev.2019.04.015

Guimarães FS, Rocha de Oliveira AL, Amorim LED, Rios FJ, Lehmann B, Hernández CR, Moraes R (2021) Lithium-mica composition as pathfinder and recorder of Grenvillian-age greisenization, Rondonia Tin Province. Brazil Geochemistry 81:125737. https://doi.org/10.1016/j.chemer.2020.125737

Halliday AN (1980) The timing of early and main stage ore mineralization in Southwest Cornwall. Econ Geol 75:752–759. https://doi.org/10.2113/gsecongeo.75.5.752

Halter WE, Williams-Jones AE, Kontak DJ (1996) The role of greisenization in cassiterite precipitation at the East Kemptville tin deposit, Nova Scotia. Econ Geol 91:368–385. https://doi.org/10.2113/gsecongeo.91.2.368

Harry P (1912) On the occurrence of tin in Nova Scotia. Proceed Nova Scotian Inst Sci 12:1906–1910

Henderson CMB, Martin JS, Mason RA (1989) Compositional relations in Li-micas from SW England and France: an ion-and electron-microprobe study. Mineral Mag 53:427–449. https://doi.org/10.1180/minmag.1989.053.372.03

Henley S (1974) Geochemistry and petrogenesis of elvan dykes in the Perranporth area, Cornwall. Proc Ussher Society 3:136–145

Hulsbosch N, Boiron C, Dewaele S, Muchez P (2016) Fluid fractionation of tungsten during granite–pegmatite differentiation and the metal source of peribatholitic W quartz veins: evidence from the Karagwe-Ankole Belt (Rwanda). Geochim Cosmochim Acta 175:299–318. https://doi.org/10.1016/j.gca.2015.11.020

Icenhower J, London D (1995) An experimental study of element partitioning among biotite, muscovite, and coexisting peraluminous silicic melt at 200 MPa (H_2O). Am Min 11–12:1229–1251. https://doi.org/10.2138/am-1995-11-1213

Ilton ES, Veblen DR (1988) Copper inclusions in sheet silicates from porphyry Cu deposits. Nature 334:516–518. https://doi.org/10.1038/334516a0

Ilton ES, Veblen DR (1993) Origin and mode of copper enrichment in biotite from rocks associated with porphyry copper deposits; a transmission electron microscopy investigation. Econ Geol 88:885–900. https://doi.org/10.2113/gsecongeo.88.4.885

Ilton ES, Earley D, Marozas DC, Veblen DR (1992) Reaction of some trioctahedral micas with copper sulfate solutions at 25 degrees C and 1 atmosphere; an electron microprobe and TEM investigation. Econ Geol 87:1813–1829. https://doi.org/10.2113/gsecongeo.87.7.1813

Jackson NJ, Moore JMCM, Rankin AH (1977) Fluid inclusions and mineralization at Cligga Head, Cornwall, England. J Geol Soc 134:343–349. https://doi.org/10.1144/gsjgs.134.3.0343

Johan Z, Strnad L, Johan V (2012) Evolution of the Cínovec (Zinnwald) granite cupola, Czech Republic: composition of feldspars and micas, a clue to origin of W, Sn mineralization. Can Mineral 50:1131–1148. https://doi.org/10.3749/canmin.50.4.1131

Kroner U, Hahn T, Romer RL, Linnemann U (2007) The Variscan orogeny in the Saxo-Thuringian zone-heterogenous overprint of Cadomian/Paleozoic Peri-Gondwana crust. Special Papers Geol Soc Am 423:153. https://doi.org/10.1130/2007.2423(06)

Legros H, Marignac C, Mercadier J, Cuney M, Richard A, Wang RC, Charles N, Lespinasse MY (2016) Detailed paragenesis and Li-mica compositions as recorders of the magmatic-hydrothermal evolution of the Maoping W-Sn deposit (Jiangxi, China). Lithos 264:108–124. https://doi.org/10.1016/j.lithos.2016.08.022

Lehmann B (1990) Metallogeny of tin. Metallogeny of tin. Springer-Verlag, Berlin

Lehmann B (2021) Formation of tin ore deposits: a reassessment. Lithos 402:105756. https://doi.org/10.1016/j.lithos.2020.105756

Loïs M, Salvi S, Melleton J, Lach P, Pochon A, Bailly L, Béziat D, De Parseval P (2022) Mica trace-element signatures: highlighting superimposed W-Sn mineralizations and fluid sources. Chem Geol 600:120866. https://doi.org/10.1016/j.chemgeo.2022.120866

London D (1986) Magmatic-hydrothermal transition in the Tanco rare-element pegmatite: evidence from fluid inclusions and phase-equilibrium experiments. Am Min 71:376–395

London D (2022) A Rayleigh model of cesium fractionation in granite-pegmatite systems. Am Min 107:82–91. https://doi.org/10.2138/am-2021-7855

London D, Manning DAC (1995) Chemical variation and significance of tourmaline from southwest England. Econ Geol 90:495–519. https://doi.org/10.2113/gsecongeo.90.3.495

Manning DAC, Hill PI, Howe JH (1996) Primary lithological variation in the kaolinized St Austell granite, Cornwall, England. J Geol Soc 153:827–838. https://doi.org/10.1144/gsjgs.153.6.0827

Martín-Fernandez JA, Barcelo-Vidal C, Pawlowsky-Glahn V (2003) Dealing with zeros and missing values in compositional data sets using nonparametric imputation. Math Geol 35:253–278. https://doi.org/10.1023/A:1023866030544

Martins T, Encarnación RR, Alexandre LIMA, de Parseval P (2012) Geochemistry and evolution of micas in the Barroso-Alvão

pegmatite field, Northern Portugal. Can Mineral 50:1117–1129. https://doi.org/10.3749/canmin.50.4.1117
Meunier A, Velde B (1982) Phengitization, sericitization and potassium-beidellite in a hydrothermally-altered granite. Clay Miner 17:285–299
Michaud JAS, Pichavant M, Villaros A (2021) Rare elements enrichment in crustal peraluminous magmas: insights from partial melting experiments. Contrib to Mineral Petrol 176:1–33. https://doi.org/10.1007/s00410-021-01855-9
Monnier L, Salvi S, Melleton J, Lach P, Pochon A, Bailly L, Béziat D, De Parseval P (2022) Mica trace-element signatures: Highlighting superimposed W-Sn mineralizations and fluid sources. Chem Geol 600:120866. https://doi.org/10.1016/j.chemgeo.2022.120866
Müller A, Seltmann R, Halls C, Siebel W, Dulski P, Jeffries T, Spratt J, Kronz A (2006) The magmatic evolution of the Land's End pluton, Cornwall, and associated pre-enrichment of metals. Ore Geol Rev 28:329–367. https://doi.org/10.1016/j.oregeorev.2005.05.002
Petrone CM, Mollo S, Gertisser R, Buret Y, Scarlato P, Del Bello E, Andronico D et al (2022) Magma recharge and mush rejuvenation drive paroxysmal activity at Stromboli volcano. Nat Comm 13:7717. https://doi.org/10.1038/s41467-022-35405-z
Pichavant M (1981) An experimental study of the effect of boron on a water saturated haplogranite at I kbar vapour pressure. Contrib to Mineral Petrol 76:430–439. https://doi.org/10.1007/BF00371485
Pichavant M (2022) Experimental crystallization of the beauvoir granite as a model for the evolution of variscan rare metal magmas. J Petrol 63:egac120. https://doi.org/10.1093/petrology/egac120
Psyrillos A, Manning DAC, Burley SD (2001) The nature and significance of illite associated with quartz-hematite hydrothermal veins in the St. Austell pluton, Cornwall. England Clay Minerals 36:585–597. https://doi.org/10.1180/0009855013640011
Reimann C, Filzmoser P, Garrett R, Dutter R (2011) Statistical data analysis explained: applied environmental statistics with R. John Wiley & Sons, Hoboken, NJ, USA
Roda Robles E, Pesquera A, Gil PP, Torres-Ruiz J, De Parseval P (2006) Mineralogy and geochemistry of micas from the Pinilla de fermoselle pegmatite (Zamora, Spain). Eur J Mineral 8:369–377. https://doi.org/10.1127/0935-1221/2006/0018-0369
Šala M, Šelih VS, Stremtan CC, Tămaş T, van Elteren JT (2021) Implications of laser shot dosage on image quality in LA-ICP-QMS imaging. J Anal at Spectrom 36:75–79. https://doi.org/10.1039/D0JA00381F
Sanderson DJ (1984) Structural variation across the northern margin of the Variscides in NW Europe. In: Hutton, DHW, Sanderson DJ (Eds): Variscan tectonics of the North Atlantic Region. Special Publication of the Geol Soc Lond 14:149–165. https://doi.org/10.1144/GSL.SP.1984.014.01.15
Scrivener RC (2006) Cornubian granites and mineralisation of SWEngland. In: Brenchley PJ, Rawson, PF (Eds.), The geology of England and Wales, 2nd ed. Geol Soc Lond 257–268. https://doi.org/10.1144/GOEWP.11
Shail RK, Leveridge BE (2009) The Rhenohercynian passive margin of SW England: development, inversion and extensional reactivation. C R Geosci 341:140–155. https://doi.org/10.1016/j.crte.2008.11.002
Shail RK, Wilkinson JJ (1994) Late- to Post-Variscan Extensional Tectonics in South Cornwall Proceedings of the Ussher Society 8:262–270
Shaw R (2022) The potential for lithium in the UK. British Geological Survey Commissioned Report, CR/22/123, p 8. https://nora.nerc.ac.uk/id/eprint/535661/
Sheppard SMF (1977) The Cornubian batholith, SW England: D/H and 18O/16O studies of kaolinite and other alteration minerals. J Geol Soc London 133:573–591. https://doi.org/10.1144/gsjgs.133.6.0573
Simons B, Shail RK, Andersen JCØ (2016) The petrogenesis of the Early Permian Variscan granites of the Cornubian Batholith: lower plate post-collisional peraluminous magmatism in the Rhenohercynian Zone of SW England. Lithos 260:76–94. https://doi.org/10.1016/j.lithos.2016.05.010
Simons B, Andersen JCØ, Shail RK, Jenner FE (2017) Fractionation of Li, Be, Ga, Nb, Ta, In, Sn, Sb, W and Bi in the peraluminous early permian Variscan granites of the Cornubian Batholith: precursor processes to magmatic-hydrothermal mineralisation. Lithos 278:491–512. https://doi.org/10.1016/j.lithos.2017.02.007
Stone M (1992) The Tregonning Granite: petrogenesis of Li-mica granites in the Cornubian Batholith. Mineral Mag 56:141–155. https://doi.org/10.1180/minmag.1992.056.383.01
Stone M, Exley CS, George MC (1988) Compositions of trioctahedral micas in the Cornubian batholith. Mineral Mag 52:175–192. https://doi.org/10.1180/minmag.1988.052.365.04
Suárez S, Nieto F, Velasco F, Martín FJ (2011) Serpentine and chlorite as effective Ni-Cu sinks during weathering of the Aguablanca sulphide deposit (SW Spain). TEM evidence for metal-retention mechanisms in sheet silicates. Eur J Mineral 23:179–196. https://doi.org/10.1127/0935-1221/2011/0023-2084
Tischendorf G, Gottesmann B, Förster HJ, Trumbull RB (1997) On Li-bearing micas: estimating Li from electron microprobe analyses and an improved diagram for graphical representation. Mineral Mag 61:809–834. https://doi.org/10.1180/minmag.1997.061.409.05
Tischendorf G, Förster HJ, Gottesmann B (2001) Minor-and trace-element composition of trioctahedral micas: a review. Mineral Mag 65:249–276. https://doi.org/10.1180/0026461015502 44
Uwanyirigira J (2018) Mineralogical, petrogenetic, and geochemical characteristics of the Meldon Aplite and its implications to Cornwall and Devon for rare-element pegmatite exploration. http://hdl.handle.net/123456789/513
van Elteren JT, Šelih VS, Šala M (2019) Insights into the selection of 2D LA-ICP-MS (multi) elemental mapping conditions. J Anal at Spectrom 34:1919–1931. https://doi.org/10.1039/C9JA00166B
Van Malderen SJM, van Elteren JT, Šelih VS, Vanhaecke F (2018) Considerations on data acquisition in laser ablation-inductively coupled plasma-mass spectrometry with low-dispersion interfaces. Spectrochim Acta Part B 140:29–34. https://doi.org/10.1016/j.sab.2017.11.007
Ward CD, McArthur JM, Walsh JN (1992) Rare earth element behaviour during evolution and alteration of the Dartmoor Granite, SW England. J Petrol 33:785–815. https://doi.org/10.1093/petrology/33.4.785
Wilkinson JJ (1990) The role of metamorphic fluids in the development of the Cornubian orefield: fluid inclusion evidence from south Cornwall. Mineral Mag 54:219–230. https://doi.org/10.1180/minmag.1990.054.375.08
Williamson BJ, Stanley CJ, Wilkinson JJ (1997) Implications from inclusions in topaz for greisenisation and mineralisation in the Hensbarrow topaz granite, Cornwall, England. Contrib to Mineral Petrol 127:119–128. https://doi.org/10.1007/s004100050269
Williamson BJ, Müller A, Shail RK (2010) Source and partitioning of B and Sn in the Cornubian batholith of southwest England. Ore Geol Rev 38:1–8. https://doi.org/10.1016/j.oregeorev.2010.05.002
Willis-Richards J, Jackson NJ (1989) Evolution of the Cornubian ore field, Southwest England; Part I, Batholith modeling and ore distribution. Econ Geol 84:1078–1100. https://doi.org/10.2113/gsecongeo.84.5.1078
Yang Z, Wang R, Che X, Yin R, Xie L, Hu H (2020) Formation of columbite and microlite after alteration of Nb-and Ta-bearing biotite from the Lizaizhai pegmatite (Guangning ore district, Guangdong, South China): identification of a new potential Nb–Ta mineralization type. J Asian Earth Sciences 190:104154. https://doi.org/10.1016/j.jseaes.2019.104154
Zhu Z, Wang R, Marignac C, Cuney M, Mercadier J, Che X, Lespinasse MY (2018) A new style of rare metal granite with Nb-rich mica: the Early Cretaceous Huangshan rare-metal granite suite, northeast Jiangxi Province, southeast China. Am Min 103:1530–1544. https://doi.org/10.2138/am-2018-6511